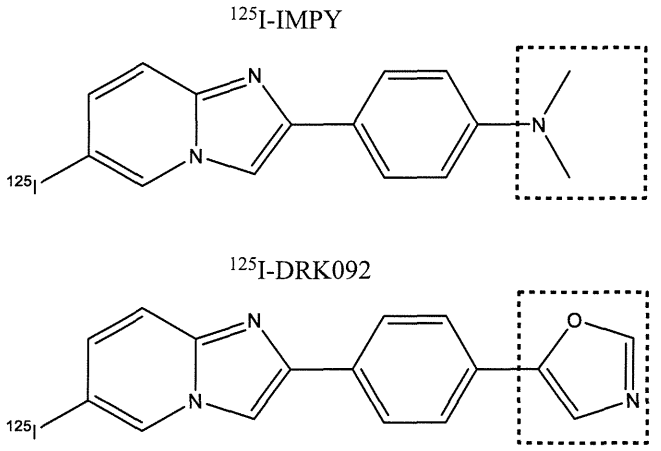

Fig. 1. Chemical structures of ^{125}I-DRK092 and ^{125}I-IMPY. Squares enclosed by dotted lines indicate the -NMe_2 group and the oxazole ring in chemical structures of IMPY and DRK092, respectively.

coronal sections by cryostat microtome (Carl Zeiss, Jena, Germany). These brain sections were closely attached to the imaging plate for an optimized contact period and scanned by FLA3000 system (GE Healthcare). Region of interests (ROIs) were carefully placed on indicated brain regions with reference to a brain atlas (The Mouse Brain in Stereotaxic Coordinates, Paxinos G and Franklin KBJ, Second Edition, Academic Press, San Diego, 2001). The counterstaining of plaques with Congo Red was performed in the same brains sections according to a well-established method after autoradiogram.

3. Results and discussion

3.1. In vitro binding parameters

With a most advanced SPECT ligand, ex vivo autography with ^{125}I-IMPY has successfully visualized Aβ deposition in AD model mouse [13]. However, it still lacks sufficient ability to distinguish patients with AD from cognitively normal subjects in SPECT scans. Metabolic instability, insufficient affinity for fibrillary Aβ and brain permeability are considered to be responsible for its limited application in human subjects [14]. Thus, more improvements are needed for further clinical applications. Replacement of the -NMe_2 group in the chemical structure of IMPY with the oxazole ring resulted in DRK092 (Fig. 1). The half-maximal inhibitory concentration (IC_{50}) values of several well-known amyloid ligands including IMPY, Pittsburgh Compound-B (PiB), 2-(1-{6-[(2-fluoroethyl)(methyl)amino]-2-naphthyl}ethylidene)malononitrile (FDDNP), Congo Red and Thioflavin T are shown in Supplementary Information, where DRK092 showed higher affinity for synthetic human Aβ fibrils than these compounds. Binding parameter analyses using a two-site binding model also demonstrated that the affinity of DRK092 for synthetic human Aβ(1-40) fibrils, and brain homogenates of Tg mice and AD patients was approximately 2.4–18 times higher than that of IMPY (Table 1). Thus, replacement of the -NMe_2 group with the oxazole ring seems to improve the affinity for Aβ deposition. To the best of our knowledge, no published data demonstrated that such replacement leaded to improve the affinity for Aβ deposition. In addition, such modification in chemical structure also decreased the lipophilic parameter (LogD) from approximately 4.03 (IMPY) to 3.64 (DRK092) [15]. These results provide important information for strategies for imaging agent discovery, because many amyloid imaging agents have the -NMe_2 group in their chemical structures with different scaffolds, such as ^{18}F-BF227 and ^{18}F-FACT, which showed limited utility for the detection of Aβ deposition in human subjects likely due to their relatively high lipophilicity [17,18], and such modification may be helpful for improving affinity and lipophilicity.

3.2. Biodistribution of ^{125}I-DRK092 in normal rats

Biodistribution analysis demonstrated that, in the initial phase, ^{125}I-DRK092 was mainly accumulated in lung, kidney and liver among peripheral organs. Notably, no relevant abnormal accumulation in specific organs was measured during the observation period after the bolus injection, confirming that the use of DRK092 should not give rise to safety concerns regarding abnormal distribution. There was only a slight increase in thyroid uptake within 40 min, suggesting that there need be little worry about de-iodination of ^{125}I-DRK092 in further SPECT imaging in short-term scans. Measured brain-to-blood ratios were approximately 3.2, 3.2, 1.3, 0.6, and 0.4 at 2, 5, 20, 40, and 90 min post-injection, respectively (Table 2), much higher than those of ^{125}I-IMPY (approximately 0.15, 0.04 and 0.02 at 2, 30 and 60 min post-injection, respectively) as reported in previous studies [13].

3.3. In vitro autoradiographic analysis

Since Aβ plaques in patients with AD may be structurally different from those in Tg mouse [2,19], we performed in vitro autoradiography with ^{125}I-DRK092 using both Tg (Tg2576) mouse and patient with AD tissues to confirm its binding to Aβ deposited in the brains of Tg mouse and AD patient. More evident radio-signals were captured in the cortical/hippocampal area and gray matter of the temporal cortical area, usually enriched with Aβ deposition, in Tg (Tg2576) mouse and AD brains, respectively, as compared with the corresponding areas in non-Tg mouse and healthy control (HC). The addition of non-radiolabeled DRM106 significantly blocked the binding of ^{125}I-DRK092 in Tg (Tg2576) and AD brain sections, but not in non-Tg and HC brains, indicating that these were amyloidosis-associated specific binding, although there were few detectable plaque-like radio-signals remaining in the subiculum of Tg mouse. In addition to those plaque-associated radiolabelings, there were also distinct lipophilic non-specific bindings to myelin-rich regions in mouse and human tissues (Fig. 2).

3.4. Ex vivo autoradiographic detection of Aβ deposition with ^{125}I-DRK092 and ^{125}I-IMPY

Ex vivo autoradiographic images have clearly demonstrated that the brain uptake of either ^{125}I-IMPY or ^{125}I-DRK092 decreased with time after an initial peak, and there was appreciable Aβ plaque-associated accumulation of these two radioligands in the cortices of Tg, but not non-Tg mice, within 2 h post-injection. However, the labeling of ^{125}I-IMPY on Aβ plaques became very weak and finally invisible by 5–8 h post-injection. In contrast, the labeling of ^{125}I-DRK092 on Aβ plaques was still appreciable even after 8 h. Unlike the in vitro autoradiographic images, there was little lipophilic non-specific binding of ^{125}I-DRK092 in the corpus callosum (Fig. 3A). Although the ratio of signals in cortex-to-striatum (CT-to-ST ratio), as plaque-rich and reference tissues, respectively, of ^{125}I-DRK092 seemed not to overly differentiate from that of ^{125}I-IMPY in Tg mouse, radioactivity of ^{125}I-DRK092 remaining in brains of both Tg and non-Tg mice was much higher than that of ^{125}I-IMPY at all time points examined (Fig. 3B), likely due to its higher brain uptake and affinity for Aβ aggregates. The amyloid deposit-associated ^{125}I-DRK092 labeling was further confirmed by subsequent counterstaining with Congo Red (Fig. 3C and D). The above observations provided explicit evidence that ^{125}I-DRK092 has improved detectability of Aβ plaques as compared with ^{125}I-IMPY. Higher brain retention without negative effect on

Table 1
Binding parameters.

Sample	High-affinity binding site				Low-affinity binding site			
	^{125}I-IMPY		^{125}I-DRK092		^{125}I-IMPY[c]		^{125}I-DRK092	
	[a]K_d	[b]B_{max}	K_d	B_{max}	K_d	B_{max}	K_d	B_{max}
Aβ1-40 fibrils	1.14 ± 0.36	0.14 ± 0.03	0.28 ± 0.20	0.041 ± 0.03	24.65 ± 1.27	1.47 ± 0.02	2.56 ± 0.13	1.01 ± 0.02
Tg brain	13.18 ± 2.58	8.40 ± 2.25	0.73 ± 0.73	0.44 ± 0.63	1107 ± 451	7848 ± 2648	14.90 ± 3.06	59.30 ± 10.80
AD brain	4.58 ± 0.65	1.99 ± 0.11	1.87 ± 0.17	1.66 ± 0.08	–	–	97.40 ± 11.28	3.56 ± 0.08

The data of Aβ fibrils, Tg brain (20-month-old), and AD brain (89-year-old) were mean ± standard errors of duplicate experiments.
[a] K_d was expressed as nM.
[b] B_{max} for Aβ fibrils and mouse/human tissues were expressed as pmol/nmol of Aβ and pmol/g tissue, respectively.
[c] Only one binding site was detected in curve-fitting analysis of ^{125}I-IMPY.

Table 2
Biodistribution of [^{125}I]DRK092 in normal rats.

Organ	2 min	5 min	20 min	40 min	90 min	180 min	360 min	1440 min
% ID/g tissue (mean ± SD; n = 3)								
Blood	0.29 ± 0.03	0.25 ± 0.00	0.23 ± 0.02	0.24 ± 0.01	0.22 ± 0.03	0.24 ± 0.02	0.31 ± 0.15	0.12 ± 0.01
Brain	0.92 ± 0.10	0.81 ± 0.05	0.30 ± 0.04	0.14 ± 0.00	0.08 ± 0.01	0.05 ± 0.00	0.05 ± 0.02	0.02 ± 0.00
Heart	0.82 ± 0.07	0.57 ± 0.06	0.36 ± 0.03	0.27 ± 0.01	0.22 ± 0.04	0.21 ± 0.02	0.21 ± 0.09	0.09 ± 0.01
Lung	1.36 ± 0.18	1.27 ± 0.11	0.76 ± 0.11	0.59 ± 0.04	0.49 ± 0.07	0.42 ± 0.05	0.42 ± 0.19	0.20 ± 0.01
Liver	0.94 ± 0.22	1.48 ± 0.27	1.10 ± 0.16	0.74 ± 0.05	0.54 ± 0.05	0.40 ± 0.01	0.38 ± 0.17	0.20 ± 0.01
Spleen	0.61 ± 0.08	0.53 ± 0.03	0.31 ± 0.03	0.24 ± 0.00	0.18 ± 0.01	0.17 ± 0.01	0.20 ± 0.07	0.08 ± 0.01
Kidney	2.89 ± 0.07	2.02 ± 0.07	1.29 ± 0.16	0.79 ± 0.04	0.55 ± 0.07	0.42 ± 0.03	0.40 ± 0.18	0.16 ± 0.02
% ID (mean ± SD; n = 3)								
Thyroid gland	0.08 ± 0.00	0.07 ± 0.00	0.10 ± 0.02	0.18 ± 0.01	0.40 ± 0.01	0.83 ± 0.10	1.56 ± 0.35	3.75 ± 0.34

Normal Sprague-Dawley (SD) rats (8 weeks old; Charles River Laboratories Japan Inc., Yokohama, Japan) were administered with [^{125}I]DRK092 (1.85 MBq/kg body weight) via the tail vein, and following processes were performed as described in our previous publication [15].

signal-to-noise ratio would provide more intense radio-signals and therefore be beneficial for clearer imaging, and also allow lower injection doses and resultant attenuation of radiation exposure for acquirement of similar-quality images. Very recently, SPECT imaging with a radioiodine-labeled pyridyl benzofuran derivative was reported to successfully visualize amyloid deposited in living Tg2576 mice [9]. This compound showed approximately 3-fold higher affinity for fibrillary Aβ than IMPY as estimated with inhibition constants for the binding of ^{125}I-IMPY to human synthetic Aβ aggregate [9]. Although we have not validated the utility of radiolabeled DRK092 for SPECT imaging in living brains, brain-permeability and affinity for Aβ deposits (approximately from 2.4- to 24-fold higher than IMPY as estimated with K_d or IC_{50} in various samples; Table 1 and Supplementary Information) seem sufficient for in vivo SPECT imaging. Additionally, the ratio of radioactivity remaining in normal brain at 2 min to that at 60 min ($brain_{2/60\,min}$ ratio) post-injection of radioiodinated pyridyl benzofuran derivative was approximately 0.3 [9], much higher than that of ^{125}I-DRK092 ($brain_{2/60\,min}$ ratio was estimated at between 0.15 and 0.09; Table 2). These numerical data were consistent with high- and low-level lipophilic non-specific bindings to myelin-rich areas, such as the corpus callosum and internal capsule, in ex vivo autoradiographic images with radioiodinated pyridyl benzofuran derivative [9], and ^{125}I-DRK092 (Fig. 3A), respectively.

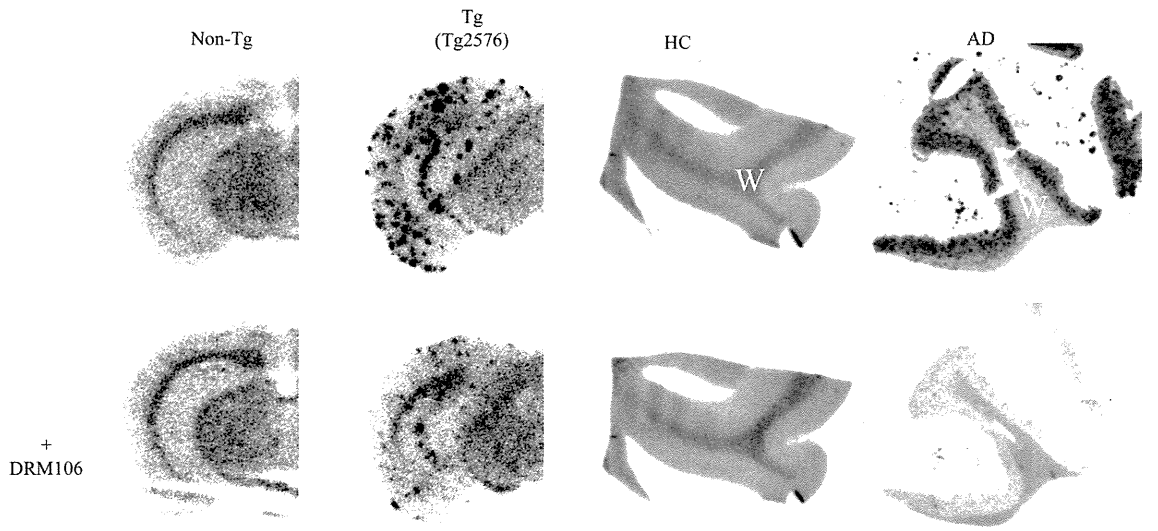

Fig. 2. In vitro autoradiographic images of ^{125}I-DRK092. The brain sections were from 23-month-old non-Tg, Tg mice, healthy control (HC) and AD from left to right, in the absence (upper) and presence (lower) of non-radiolabeled DRM106 (10 μM). Non-specific binding was defined in the presence of non-radiolabeled DRM106. W: white matter.

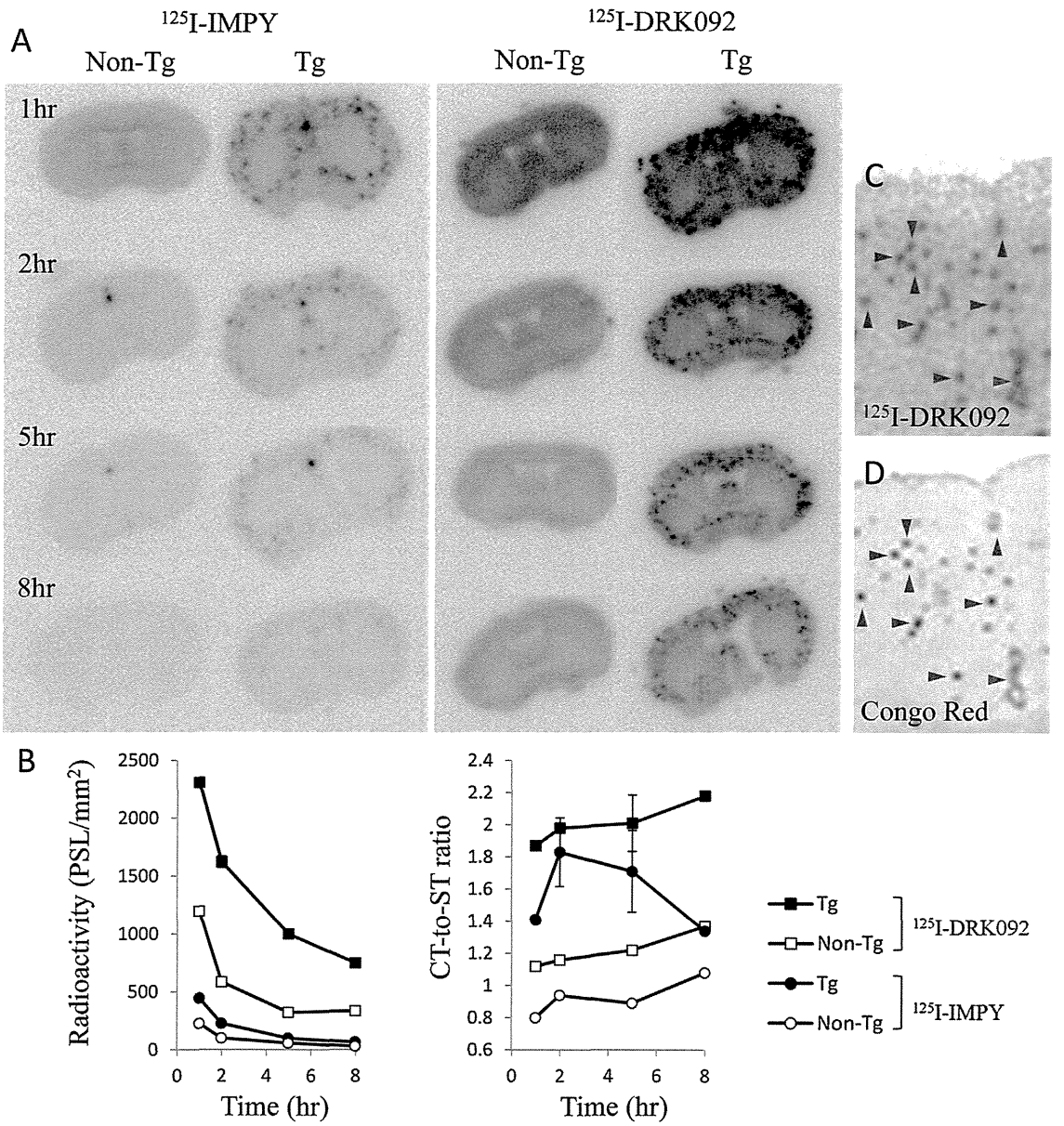

Fig. 3. Ex vivo autoradiographic analysis of ^{125}I-DRK092 and ^{125}I-IMPY in Tg mouse brains. (A and B) The representative coronal images (approximately 0.2–0.8 mm anterior to the bregma) of 19-month-old male Tg and age-matched non-Tg mice having received bolus injection of radiolabeled ^{125}I-DRK092 and ^{125}I-IMPY at 1, 2, 5, and 8 h post-injection are shown in Panel A. Quantitative analyses of radioactivity in cortical areas (left; radioactivity was estimated as photostimulated luminescence (PSL) per mm^2) and cortex-to-striatum (CT-to-ST) ratios of radioactivity (right) of Tg (closed symbols, $n = 2$ for data at 2 and 5 h, $n = 1$ for data at 1 and 8 h post-injection) and non-Tg mice (open symbols, $n = 1$ for each time point) administered with ^{125}I-DRK092 (squares) and ^{125}I-IMPY (circles) are shown in Panel B. Vertical bars in graph denote SD. (C and D) Co-localization of ^{125}I-DRK092 accumulation (C) and counterstaining of plaques with Congo Red (D). The same brain section was stained with Congo Red after autoradiography. Red and blue arrowheads indicate Aβ plaques and cerebrovascular Aβ deposits, respectively. (For interpretation of the references to color in this figure legend, the reader is referred to the web version of the article.)

All the data presented above lead us to draw the conclusion that radioiodinated DRK092 is a potential SPECT ligand for amyloid imaging in AD.

Acknowledgments

The authors thank Prof. John Q. Trojanowski and Prof. Virginia M.-Y. Lee (Center for Neurodegenerative Disease Research, University of Pennsylvania) for kindly providing human tissue. This work was supported in part by Grants-in-Aid for Japan Advanced Molecular Imaging Program and Core Research for Evolutional Science and Technology (T. S.), and Scientific Research on Innovative Areas ("Brain Environment") 23111009 (M. H.) from the Ministry of Education, Culture, Sports, Science and Technology, Japan.

Appendix A. Supplementary data

Supplementary data associated with this article can be found, in the online version, at http://dx.doi.org/10.1016/j.neulet.2014.08.036.

References

[1] H. Braak, E. Braak, Neuropathological stageing of Alzheimer-related changes, Acta Neuropathol. (Berl) 82 (1991) 239–259.
[2] J. Maeda, B. Ji, T. Irie, T. Tomiyama, M. Maruyama, T. Okauchi, M. Staufenbiel, N. Iwata, M. Ono, T.C. Saido, K. Suzuki, H. Mori, M. Higuchi, T. Suhara, Longitudinal, quantitative assessment of amyloid, neuroinflammation, and anti-amyloid treatment in a living mouse model of Alzheimer's disease enabled by positron emission tomography, J. Neurosci. 27 (2007) 10957–10968.

[3] W.E. Klunk, H. Engler, A. Nordberg, Y. Wang, G. Blomqvist, D.P. Holt, M. Bergstrom, I. Savitcheva, G.F. Huang, S. Estrada, B. Ausen, M.L. Debnath, J. Barletta, J.C. Price, J. Sandell, B.J. Lopresti, A. Wall, P. Koivisto, G. Antoni, C.A. Mathis, B. Langstrom, Imaging brain amyloid in Alzheimer's disease with Pittsburgh Compound-B, Ann. Neurol. 55 (2004) 306–319.
[4] V. Camus, P. Payoux, L. Barre, B. Desgranges, T. Voisin, C. Tauber, R. La Joie, M. Tafani, C. Hommet, G. Chetelat, K. Mondon, V. de La Sayette, J.P. Cottier, E. Beaufils, M.J. Ribeiro, V. Gissot, E. Vierron, J. Vercouillie, B. Vellas, F. Eustache, D. Guilloteau, Using PET with 18F-AV-45 (florbetapir) to quantify brain amyloid load in a clinical environment, Eur. J. Nucl. Med. Mol. Imaging 39 (2012) 621–631.
[5] Z. Cselenyi, M.E. Jonhagen, A. Forsberg, C. Halldin, P. Julin, M. Schou, P. Johnstrom, K. Varnas, S. Svensson, L. Farde, Clinical validation of 18F-AZD4694, an amyloid-beta-specific PET radioligand, J. Nucl. Med. 53 (2012) 415–424.
[6] H. Watanabe, M. Ono, R. Ikeoka, M. Haratake, H. Saji, M. Nakayama, Synthesis and biological evaluation of radioiodinated 2,5-diphenyl-1,3,4-oxadiazoles for detecting beta-amyloid plaques in the brain, Bioorg. Med. Chem. 17 (2009) 6402–6406.
[7] Y. Maya, M. Ono, H. Watanabe, M. Haratake, H. Saji, M. Nakayama, Novel radioiodinated aurones as probes for SPECT imaging of beta-amyloid plaques in the brain, Bioconjug. Chem. 20 (2009) 95–101.
[8] W. Qu, M.P. Kung, C. Hou, S. Oya, H.F. Kung, Quick assembly of 1,4-diphenyltriazoles as probes targeting beta-amyloid aggregates in Alzheimer's disease, J. Med. Chem. 50 (2007) 3380–3387.
[9] M. Ono, Y. Cheng, H. Kimura, H. Watanabe, K. Matsumura, M. Yoshimura, S. Iikuni, Y. Okamoto, M. Ihara, R. Takahashi, H. Saji, Development of novel 123I-labeled pyridyl benzofuran derivatives for SPECT imaging of beta-amyloid plaques in Alzheimer's disease, PLOS ONE 8 (2013) e74104.
[10] Z.P. Zhuang, M.P. Kung, A. Wilson, C.W. Lee, K. Plossl, C. Hou, D.M. Holtzman, H.F. Kung, Structure–activity relationship of imidazo[1,2-a]pyridines as ligands for detecting beta-amyloid plaques in the brain, J. Med. Chem. 46 (2003) 237–243.
[11] A.B. Newberg, N.A. Wintering, K. Plossl, J. Hochold, M.G. Stabin, M. Watson, D. Skovronsky, C.M. Clark, M.P. Kung, H.F. Kung, Safety, biodistribution, and dosimetry of 123I-IMPY: a novel amyloid plaque-imaging agent for the diagnosis of Alzheimer's disease, J. Nucl. Med. 47 (2006) 748–754.
[12] M.P. Kung, C. Hou, Z.P. Zhuang, B. Zhang, D. Skovronsky, J.Q. Trojanowski, V.M. Lee, H.F. Kung, IMPY: an improved thioflavin-T derivative for in vivo labeling of beta-amyloid plaques, Brain Res. 956 (2002) 202–210.
[13] M.P. Kung, C. Hou, Z.P. Zhuang, A.J. Cross, D.L. Maier, H.F. Kung, Characterization of IMPY as a potential imaging agent for beta-amyloid plaques in double transgenic PSAPP mice, Eur. J. Nucl. Med. Mol. Imaging 31 (2004) 1136–1145.
[14] M.P. Kung, C.C. Weng, K.J. Lin, I.T. Hsiao, T.C. Yen, S.P. Wey, Amyloid plaque imaging from IMPY/SPECT to AV-45/PET, Chang Gung Med. J. 35 (2012) 211–218.
[15] C-J. Chen, K. Bando, H. Ashino, K. Taguchi, H. Shiraishi, O. Fujimoto, C. Kitamura, S. Mastushima, M Fujinaga, M-R. Zhang, H. Kasahara, T. Minamizawa, C. Jiang, T. Suhara, M. Higuchi, K. Yamada, B. Ji, Synthesis and biological evaluation of novel radioiodinated imidazopyridine derivatives for amyloid- imaging in Alzheimer disease, Bioorg. Med. Chem. 22 (2014) 4189–4197.
[16] Y. Nakano, G. Kondoh, T. Kudo, K. Imaizumi, M. Kato, J.I. Miyazaki, M. Tohyama, J. Takeda, M. Takeda, Accumulation of murine amyloidbeta42 in a gene-dosage-dependent manner in PS1 'knock-in' mice, Eur. J. Neurosci. 11 (1999) 2577–2581.
[17] H. Ito, H. Shinotoh, H. Shimada, M. Miyoshi, K. Yanai, N. Okamura, H. Takano, H. Takahashi, R. Arakawa, F. Kodaka, M. Ono, Y. Eguchi, M. Higuchi, T. Fukumura, T. Suhara, Imaging of amyloid deposition in human brain using positron emission tomography and [18F]FACT: comparison with [11C]PIB, Eur. J. Nucl. Med. Mol. Imaging 41 (2014) 745–754.
[18] S. Furumoto, N. Okamura, K. Furukawa, M. Tashiro, Y. Ishikawa, K. Sugi, N. Tomita, M. Waragai, R. Harada, T. Tago, R. Iwata, K. Yanai, H. Arai, Y. Kudo, A 18F-labeled BF-227 derivative as a potential radioligand for imaging dense amyloid plaques by positron emission tomography, Mol. Imaging Biol. 15 (2013) 497–506.
[19] W.E. Klunk, B.J. Lopresti, M.D. Ikonomovic, I.M. Lefterov, R.P. Koldamova, E.E. Abrahamson, M.L. Debnath, D.P. Holt, G.F. Huang, L. Shao, S.T. DeKosky, J.C. Price, C.A. Mathis, Binding of the positron emission tomography tracer Pittsburgh compound-B reflects the amount of amyloid-beta in Alzheimer's disease brain but not in transgenic mouse brain, J. Neurosci. 25 (2005) 10598–10606.

Bioorganic & Medicinal Chemistry 22 (2014) 4189–4197

Contents lists available at ScienceDirect

Bioorganic & Medicinal Chemistry

journal homepage: www.elsevier.com/locate/bmc

Synthesis and biological evaluation of novel radioiodinated imidazopyridine derivatives for amyloid-β imaging in Alzheimer's disease

Chun-Jen Chen [a,b,c], Kazunori Bando [a], Hiroki Ashino [a], Kazumi Taguchi [a], Hideaki Shiraishi [a], Osuke Fujimoto [a], Chiemi Kitamura [a], Satoshi Matsushima [a], Masayuki Fujinaga [b], Ming-Rong Zhang [b], Hiroyuki Kasahara [a], Takao Minamizawa [a], Cheng Jiang [d], Maiko Ono [b], Makoto Higuchi [b], Tetsuya Suhara [b], Kazutaka Yamada [c,†], Bin Ji [b,*]

[a] Fujifilm RI Pharma Co. LTD, Chiba, Japan
[b] Molecular Imaging Center, National Institute of Radiological Sciences, 4-9-1, Anagawa, Inage-ku, Chiba 263-8555, Japan
[c] The United Graduate School of Veterinary Science, Gifu University, Gifu, Japan
[d] School of Pharmacy, Fudan University, Shanghai, China

ARTICLE INFO

Article history:
Received 4 March 2014
Revised 20 May 2014
Accepted 21 May 2014
Available online 2 June 2014

Keywords:
Alzheimer's disease (AD)
Amyloid-β peptide (Aβ)
Autoradiography
Positron emission tomography (PET)
Single-photon emission computed tomography (SPECT)

ABSTRACT

Non-invasive detection for amyloid-β peptide (Aβ) deposition has important significance for the early diagnosis and medical intervention for Alzheimer's disease (AD). In this study, we developed a series of imidazopyridine derivatives as potential imaging agents for single-photon emission computed tomography (SPECT). Two of them, compounds DRK092 and DRM106, showed higher affinity for synthetic human Aβ 1–40 fibrils than did the well-known amyloid-imaging agent IMPY. A metabolite analysis revealed brain-permeable radioactive metabolites of ^{125}I-labeled DRK092 and IMPY; no radioactive metabolites from ^{125}I-labeled DRM106 ([^{125}I]DRM106) were detected. In addition, in vitro autoradiography clearly demonstrated specific binding of [^{125}I]DRM106 in the hippocampal region of AD enriched with Aβ plaques. Thus, our results strongly suggested that compound DRM106 can be used as an imaging agent for SPECT to detect Aβ deposition in AD brain.

1. Introduction

Alzheimer's disease (AD) is a progressive neurodegenerative disorder characterized by the appearance of amyloid-β peptide (Aβ) plaques and neurofibrillary tangles (NFTs). Since fibrillary Aβ can accumulate in the brain for decades before the appearance of AD,[1] in-vivo non-invasive detection of Aβ deposition is crucial for the early diagnosis and treatment of AD at the prodromal stage. Nuclear imaging by positron emission tomography (PET) and single-photon emission computed tomography (SPECT) are clinically applicable for functional examination, and are widely used in translational research. Amyloid imaging with PET tracers has been successfully employed in preclinical research and clinical trials.[2–5] ^{11}C-labeled Pittsburgh compound B ([^{11}C]PiB) is a widely used PET ligand that has been employed to quantitatively detect amyloid deposition in AD model animals and patients.[2,3,6] It has also been used as an imaging biomarker for AD diagnosis as well as a prognostic index for the conversion from mild cognitive impairment (MCI) to AD.[7–9] To overcome the disadvantage of the short half-life (approximately 20 min) of ^{11}C-labeled tracers, ligands labeled with ^{18}F (half-life: approximately 110 min) have also been developed for routine medical needs.[5,10–12] Two such radioligands, [^{18}F]florbetapir and [^{18}F]flutemetamol, have already been approved by the US Food and Drug Administration (FDA) as radioactive diagnostic agents to detect amyloid deposition in adult patients with cognitive impairment.

In comparison with PET, radioisotopes used in SPECT, such as ^{123}I (half-life: 13.22 h), have a longer half-life and can therefore achieve a longer distance delivery. More SPECT scanners have also been installed for routine clinical examination. Although inferior to PET in terms of sensitivity and quantitative performance, SPECT is more suitable for the primary screening of prodromal AD patients, owing to lower operating and installation costs. In the past decade, several SPECT ligands with different scaffolds have been developed

* Corresponding author. Tel.: +81 43 206 3251; fax: +81 43 253 0396.
E-mail addresses: kyamada@obihiro.ac.jp (K. Yamada), kihin@nirs.go.jp (B. Ji).
† Co-corresponding author: The United Graduate School of Veterinary Science, Gifu University, 1-1 Yanagido, Gifu City 501-1193, Japan. Tel.: +81 155 49 5395; fax: +81 155 49 5398.

http://dx.doi.org/10.1016/j.bmc.2014.05.043
0968-0896/

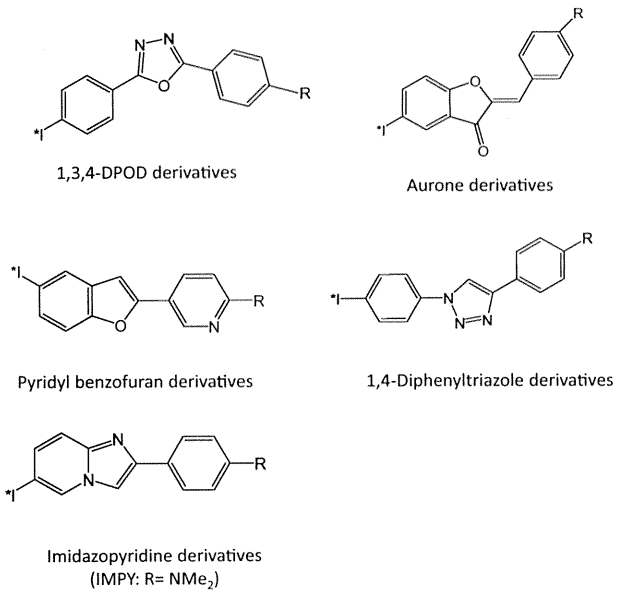

Figure 1. Basic chemical structures of radio-iodinated ligands for amyloid imaging with SPECT. *I represents radioactive iodine.

that can be used to successfully visualize amyloid deposition in brain sections of AD models and patients with AD in vitro. To date, however, there has been lack of SPECT ligands available for amyloid imaging to distinguish between normal subjects and patients with AD. In the present study, we developed a series of novel imidazopyridine derivatives to be employed as SPECT agents in the in vivo detection of Aβ pathology.

2. Results and discussion

To date, a number of iodinated ligands, such as dipheny-1,3,4-oxadiazole (1,3,4-DPOD) derivatives,[13] aurone derivatives,[14] 1,4-diphenyltriazole derivatives,[15] pyridyl benzofuran derivatives,[16] and imidazo[1,2-*a*]pyridine derivatives,[17] have been employed for amyloid imaging with SPECT (Fig. 1). IMPY, an imidazo[1,2-*a*]pyridine derivative, is the only ligand for SPECT that has been tested in human subjects.[18] Although this ligand has shown excellent properties as an imaging probe in preclinical studies,[19,20] including good brain permeability and rapid off-target washout, the preliminary clinical data failed to demonstrate the ability of this ligand to distinguish between AD and a cognitively normal brain. This may due to an insufficient affinity for Aβ fibrils or a metabolic instability.[21] In this study, novel compounds for SPECT amyloid imaging using the core structure of IMPY were developed.

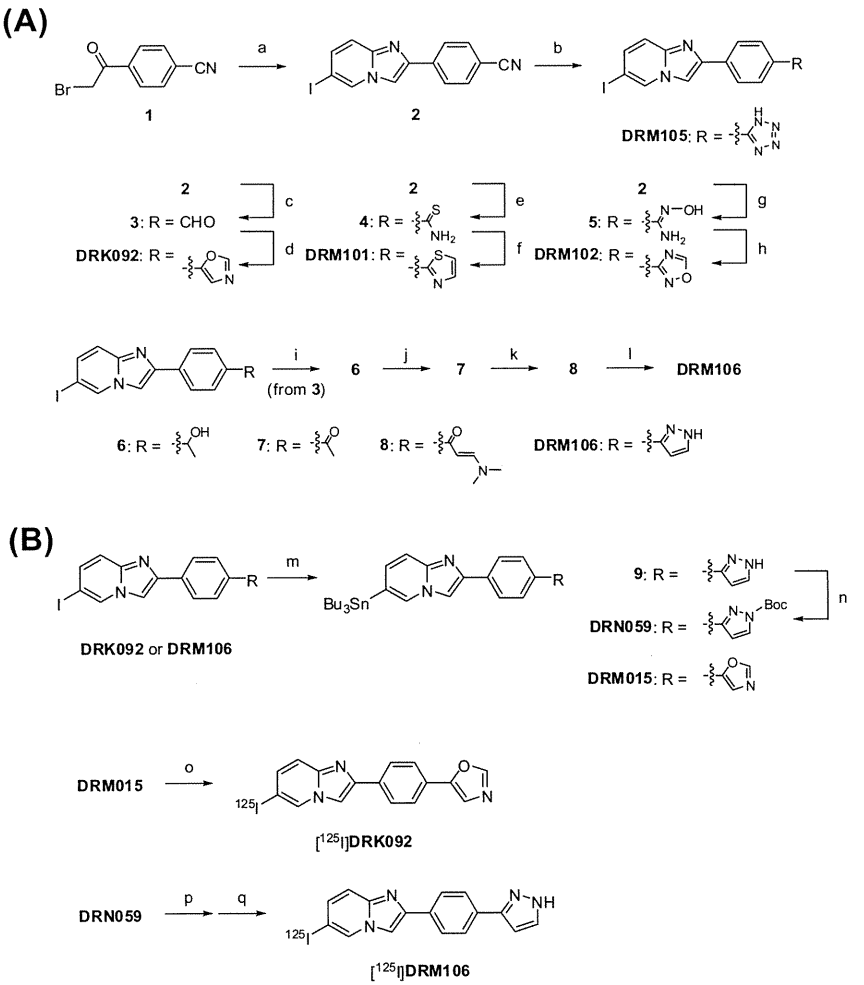

Scheme 1. Chemical synthesis and radiosynthesis: Reagents and conditions: (a) 2-amino-5-iodopyridine, $NaHCO_3$, EtOH, reflux, 16 h, 81%; (b) $Al(CH_3)_3$, Me_3SiN_3, toluene, 80 °C, 2 h, 15%; (c) DIBAL-H, CH_2Cl_2–THF, room temperature, 4 h, 81%; (d) *p*-TosMIC, K_2CO_3, MeOH, reflux, 13 h, 46%; (e) thioacetamide, HCl, DMF, 80 °C, 4 h, 71%; (f) chloroacetaldehyde, Et_3N, EtOH, reflux, 18 h, 39%; (g) NH_2OH, K_2CO_3, MeOH, reflux, 14 h, 74%; (h) $CH(OMe)_3$, reflux, 18 h, 80%; (i) MeMgBr, THF, room temperature, 5 h, 63%; (j) MnO_2, $CHCl_3$, reflux, 8 h, 64%; (k) DMFDMA, DMF, 150 °C, 16 h, 48%; (l) $NH_2NH_2{\cdot}H_2O$, EtOH, reflux, 3 h, 92%; (m) $Pd(PPh_3)_4$, $(SnBu_3)_2$, dioxane, reflux, 14–16 h, 42–49%; (n) Boc_2O, DMAP, CH_2Cl_2, room temperature, 8 h, 93%; (o) chloramine T, Na[^{125}I], 0.3 M PBS, room temperature, 5 min; (p) 12 N NaOH, EtOH, 70 °C, 35 min; (q) chloramine T, Na[^{125}I], 0.3 M PBS, room temperature, 2 min.

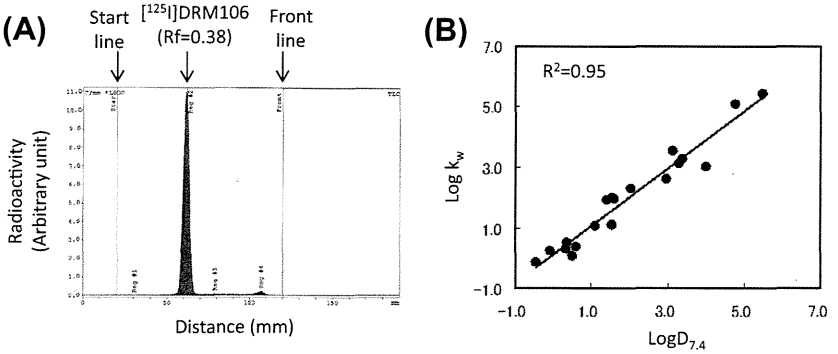

Figure 2. Thin-layer chromatography (TLC) chart employed for the analysis of the radiochemistry purity of [^{125}I]DRM106 (A); standard curve for estimation of log$D_{7.4}$ (B).

The novel imidazo[1,2-*a*]pyridine derivatives were synthesized from bromoketone **1** as shown in Scheme 1. Synthesis of **2** bearing imidazo[1,2-*a*]pyridine skeleton was achieved by reaction of bromoketone **1** with 2-aminopyridines under mild basic conditions. The cyano derivative **2** was used as a common intermediate in the synthesis of DRM105, DRK092, DRM101, and DRM102. The tetrazol derivative DRM105 was synthesized by reaction of azidotrimethylsilane with trimethylaluminum used as a catalyst. Transformation of cyano derivative **2** into **3** with DAIBAL-H, followed by treatment with *p*-toluenesulfonylmethylisocyanide, gave DRK092. The thioamidation of **2** with thioacetamide under acidic conditions led to the formation of **4**, which was treated with chloroacetaldehyde in the presence of Et_3N to produce the thiazole derivative DRM101. In addition, reaction of **2** with hydroxylamine produced amidine derivatives **5**, followed by cyclization of amidine **5** with trimethylorthoformate leading to the oxadiazole derivative DRM102. Additional reaction of aldehyde **3** with methylmagnesium bromide produced the alcohol derivative **6**, which was treated with manganese dioxide to give the acetyl derivatives **7**. Condensation of the acetyl derivative **7** with dimethylformamide dimethylacetal (DMFDMA) led to the synthesis of β-dimethylaminovinylketone derivatives **8**, and subsequent cyclization of the β-dimethylaminovinylketone group with hydrazine produced DRM106.

The precursors for radioiodination, tributyltin derivatives DRM015 and DRN059, were synthesized by stannylation of iododerivatives DRK092 or DRM106 with bis(tributyltin) in the presence of tetrakis(triphenylphosphine)palladium(0) [Pd(PPh_3)$_4$] and subsequent treatment of **9** with Boc_2O. Synthesis of [^{125}I]DRK092 and [^{125}I]DRM106 was carried out as shown in Scheme 1. The [^{125}I]iodination of the tributylstannyl precursors DRM015 or DRN059 with [^{125}I]NaI was performed by iododestannylation with chloramine T as a catalyst. When DRN059 was used as precursor, deprotection of the Boc group in the pyrazole ring was performed by treatment with a 12 N solution of NaOH at 70 °C for 35 min. After these reactions were completed, a semi-preparative HPLC system with a radioactive detector was used and the radioactive fraction corresponding to [^{125}I]DRK092 or [^{125}I]DRM106 collected. The eluent was diluted with water, and the solution was loaded onto a pre-conditioned C_{18} Sep-Pak light cartridge. Finally, the desired compound, [^{125}I]DRK092 or [^{125}I]DRM106, was eluted from the cartridge with EtOH to produce the final product. The successful synthesis of [^{125}I]DRK092 and [^{125}I]DRM106 was confirmed by comparison with non-radiolabeled DRK092 or DRM106 using HPLC. As for [^{125}I]DRM106 (Fig. 2A), the radiochemical purity of [^{125}I]DRK092 and [^{125}I]DRM106 was analyzed by using thin-layer chromatography (TLC). In the final products, no significant chemical impurities were found; the radiochemical purity of radioligands remained larger than 95% after keeping the products at room temperature for 24 h. Additionally, the experimental condition of radiolabeling of DRM106 was also examined by cold run as described in Supplementary information. We confirmed that the resulting product derived from NaI under the condition of cold run was DRM106 by comparing the retention time with that of synthesized standard DRM106 characterized with ^{1}H and ^{13}C NMR (Supplementary information).

Table 1
IC_{50} for binding of [^{125}I]IMPYto synthetic human Aβ (1–40) and lipophilic parameter (Log*D*)

Compounds	IC_{50} (nM)	Log*D* (pH 7.4)
DRK092	1.08	3.64
DRM101	6.87	3.06
DRM102	4.15	3.12
DRM105	744.87	1.73
DRM106	1.86	3.20
IMPY	2.93	4.03

The affinity of the imidazo[1,2-*a*]pyridine derivatives was evaluated based on the binding inhibition of [^{125}I]IMPY to synthetic human Aβ (1–40) fibrils. As shown in Table 1, the half-maximal inhibitory concentration (IC_{50}) values ranged from approximately 1–740 nM. Compounds DRK092 and DRM106 showed a higher affinity (approximately 1.1 and 1.9 nM respectively) than IMPY (approximately 2.9 nM). In addition, acetaminophen, allopurinol, antipyrine, bifonazole, caffeine, chloramphenicol, chlorpheniramine, cimetidine, clonidine, clozapine, estradiol, haloperidol, hydrocortisone, naphthalene, prednisolone, risperidone, testosterone, triphenylene, and warfarin with published log$D_{7.4}$ values were used to construct the standard curve to estimate the lipophilicity parameter.[22,23] The logarithms of the capacity factors (logk_w) of these compounds measured in this work showed a strong correlation with the log$D_{7.4}$ values reported in previous studies (Fig. 2B). As shown in Table 1, the log$D_{7.4}$ values of DRK092 and DRM106 (3.6 and 3.2, respectively) calculated from their logk_w suggest that these compounds may have suitable brain permeability properties. Further analysis of these two promising compounds was thus performed.

As expected, [^{125}I]IMPY, [^{125}I]DRK092, and [^{125}I]DRM106 showed excellent brain uptake. In particular, the initial peaks (ranging approximately between 0.8% and 1.3% of ID/g brain) were rapidly eliminated from normal rat brains (Fig. 3A). The analysis of metabolites by TLC clearly demonstrated that no detectable metabolites from [^{125}I]DRM106 in the brain over the observation period were present. In contrast, at least two metabolites from [^{125}I]DRK092 and [^{125}I]IMPY, respectively, were detected in the brain samples in the initial phase after the radiolabeled ligands were injected into normal rats (Fig. 3B–D). Within 30 min of intravenous injection in the AD mouse model[20], the percentage of intact IMPY in plasma and brain decreased to approximately 20% and 40%, respectively. This finding confirmed the poor metabolic stability of IMPY, which in turn may be one of the reasons why AD

Table 2
Biodistribution of [^{125}I]DRM106 in normal rats

Organ	% ID/g tissue (mean ± SD)								
	2 min	5 min	15 min	30 min	1 h	2 h	4 h	8 h	24 h
Blood	0.35 ± 0.02	0.29 ± 0.03	0.17 ± 0.02	0.13 ± 0.01	0.08 ± 0.01	0.07 ± 0.00	0.06 ± 0.01	0.05 ± 0.02	0.01 ± 0.00
Brain	0.45 ± 0.07	0.35 ± 0.04	0.20 ± 0.07	0.08 ± 0.02	0.02 ± 0.00	0.01 ± 0.00	0.00 ± 0.00	0.00 ± 0.00	0.00 ± 0.00
Skin	0.22 ± 0.03	0.21 ± 0.03	0.19 ± 0.01	0.15 ± 0.02	0.12 ± 0.01	0.15 ± 0.02	0.14 ± 0.00	0.14 ± 0.06	0.06 ± 0.03
Heart	0.64 ± 0.06	0.35 ± 0.03	0.17 ± 0.04	0.08 ± 0.01	0.04 ± 0.01	0.03 ± 0.01	0.02 ± 0.00	0.02 ± 0.01	0.00 ± 0.00
Lung	0.84 ± 0.04	0.56 ± 0.04	0.28 ± 0.09	0.14 ± 0.03	0.07 ± 0.02	0.05 ± 0.01	0.04 ± 0.00	0.04 ± 0.01	0.01 ± 0.00
Liver	1.56 ± 0.08	2.81 ± 0.29	1.60 ± 0.19	0.89 ± 0.06	0.15 ± 0.03	0.06 ± 0.00	0.04 ± 0.00	0.04 ± 0.01	0.01 ± 0.00
Spleen	0.51 ± 0.09	0.43 ± 0.04	0.23 ± 0.07	0.10 ± 0.02	0.04 ± 0.01	0.03 ± 0.00	0.03 ± 0.00	0.02 ± 0.01	0.01 ± 0.00
Kidney	2.24 ± 0.24	1.36 ± 0.26	0.91 ± 0.19	0.55 ± 0.06	0.18 ± 0.05	0.09 ± 0.00	0.05 ± 0.01	0.07 ± 0.03	0.01 ± 0.01
Muscle	0.42 ± 0.05	0.20 ± 0.03	0.10 ± 0.03	0.05 ± 0.01	0.01 ± 0.00	0.01 ± 0.00	0.01 ± 0.01	0.01 ± 0.00	0.00 ± 0.00
					% ID (mean ± SD)				
Thyroid gland	0.07 ± 0.01	0.05 ± 0.01	0.04 ± 0.01	0.07 ± 0.01	0.09 ± 0.01	0.20 ± 0.04	0.33 ± 0.13	0.79 ± 0.26	0.51 ± 0.22

cannot be distinguished from cognitively normal brains when IMPY is used. Our data also showed that DRK092 has a similar metabolic instability to IMPY (Fig. 3B and C). IMPY and DRK092 metabolites were not fully identified in the present study; however, considering that a metabolic enzyme-catalyzed N-demethylation is likely to occur, we speculate that the observed radioactive IMPY metabolites may include *N*-demethyl derivatives. Given the difference in chemical structure between DRK092 and DRM106, the oxazole ring of DRK092 may be the reason for its metabolic instability. Taken into account all these findings, DRM106 was selected for further investigation. The biodistribution analysis demonstrated that [^{125}I]DRM106 was mainly accumulated in kidney and liver among peripheral organs in the initial phase. Notably, no relevant abnormal accumulation in special organs was measured during the observation period after the bolus injection (Table 2), which confirmed that the use of DRM106 should not raise safety concerns regarding abnormal distribution. Thyroid uptake hardly increased with time within 1 h (Table 2), suggesting less concern about deiodination of [^{125}I]DRM106 in further SPECT imaging. After the intravenous administration, brain-to-blood ratios were measured to be approximately 1.29, 1.21, 1.18, 0.66, and 0.25 at 2, 5, 15, 30, and 60 min, respectively (Table 2); these values are higher than those measured for [^{125}I]IMPY (approximately 0.15, 0.04 and 0.02 at 2, 30, 60 min post-injection, respectively) as reported in previous studies.[20]

In addition, in vitro autoradiography showed that the binding of [^{125}I]DRM106 is higher in the hippocampal region of AD brains enriched with Aβ plaques than in the corresponding region of healthy-control (HC) brain. Furthermore, the addition of non-radiolabeled DRM106 significantly decreased these bindings, demonstrating that a specific binding of [^{125}I]DRM106 occurs (Fig. 4A). The spatial consistency of plaque counterstaining with the fluorescent dye FSB and the accumulation of [^{125}I]DRM106 clearly confirmed the specific binding of [^{125}I]DRM106 to Aβ plaques (red arrowheads in Fig. 4B–D).

3. Conclusion

In the present study, we synthesized a series of novel imidazopyridine derivatives with a chemical structure similar to that of IMPY. We obtained a promising compound (DRM106) with excellent brain permeability and a rapid off-target washout, a sufficient affinity to Aβ aggregate, and an ideal metabolic stability. These data strongly suggest that DRM106, labeled with iodine-123, can be efficiently employed as SPECT agent for the detection of the amyloid pathology in the brains of patients with AD.

4. Experiments

Melting points (mp) were measured using a micromelting point apparatus (MP-500P, Yanaco, Tokyo, Japan). ^{1}H and ^{13}C NMR spectra were recorded on a JNM-AL-400 spectrometer (JEOL; Tokyo, Japan) using tetramethylsilane as an internal standard. All chemical shifts (δ) were reported in parts per million (ppm) downfield from the standard. High-resolution (HR) fast atom bombardment–mass spectrometry (FAB–MS) was performed using a JEOL NMS-SX102 spectrometer (JEOL). Column chromatography was performed on a Wakogel C-200 (Wako Pure Chemical Industries, Ltd; Osaka, Japan). HPLC was performed using a JASCO HPLC system (JASCO; Tokyo, Japan), and effluent radioactivity was monitored using a NaI (Tl) scintillation detector system. All chemical reagents were purchased of the highest grade commercially available from Sigma-Aldrich Corporation (Milwaukee, WI), Wako Pure Chemical Industries, Ltd, or Tokyo Chemical Industries, Ltd. (Tokyo, Japan).

4.1. Chemical synthesis

4.1.1. 4-(6-Iodoimidazo[1,2-*a*]pyridin-2-yl)benzonitrile (2)

$NaHCO_3$ (382 mg, 4.55 mmol) was added to a solution of 2-amino-5-iodopyridine (1.0 g, 4.55 mmol) and **1** (1.02 g, 4.55 mmol) in EtOH (30 mL) and heated at reflux for 16 h. After having quenched the reaction mixture with water (10 mL), the resulting precipitate was collected by filtration to give **2** (1.27 g, 81%) as a pale yellow powder; ^{1}H NMR (400 MHz, DMSO-d_6) δ 7.54 (1H, d, J = 9.5 Hz), 7.62 (1H, dd, J = 1.2, 9.3 Hz), 7.94 (2H, d, J = 8.3 Hz), 8.14 (2H, d, J = 8.5 Hz), 8.56 (1H, s), 9.02 (1H, s). EI-MS *m/z*: 345 (M^+).

4.1.2. 6-Iodo-2-[4-(1*H*-1,2,3,4-tetrazol-5-yl)phenyl]imidazo[1,2-*a*]pyridine (DRM105)

Under a nitrogen atmosphere, trimethylaluminum (43.3 mg, 0.30 mmol in 150 μL toluene) and azidotrimethylsilane (42 μL, 0.32 mmol) were added to a solution of **2** (104 mg, 0.30 mmol) in dry toluene (1 mL). The reaction mixture was stirred at 80 °C for 2 h. After cooling the reaction mixture to room temperature, 1 mL of 6 M HCl was added to the solution. The resulting precipitate was collected by filtration to give DRM105 (17 mg, 15%) as a colorless powder; mp: >300 °C. ^{1}H NMR (400 MHz, DMSO-d_6) δ 7.55–7.68 (2H, m), 8.18 (4H, q, J = 8.3 Hz), 8.54 (1H, s), 9.05 (1H, s). HRMS (FAB) calcd for $C_{14}H_{10}IN_6$ (M^+), 389.0012; found: 389.0022.

4.1.3. 4-(6-Iodoimidazo[1,2-*a*]pyridin-2-yl)benzaldehyde (3)

Diisobutylaluminum hydride in hexane (7.8 mL, 1.0 M; 7.8 mmol) was added to a solution of **2** (1.27 g, 3.68 mmol) in THF (15 mL) and CH_2Cl_2 (15 mL) at 0 °C and stirred for 15 min and then at room temperature for 4 h under a nitrogen atmosphere. After the reaction mixture was quenched with saturated aqueous NH_4Cl (2 mL), the solution was stirred at room temperature for 1 h. $MgSO_4$ and diethyl ether were added to the reaction mixture and stirred for 1 h. Removal of solvent under reduced

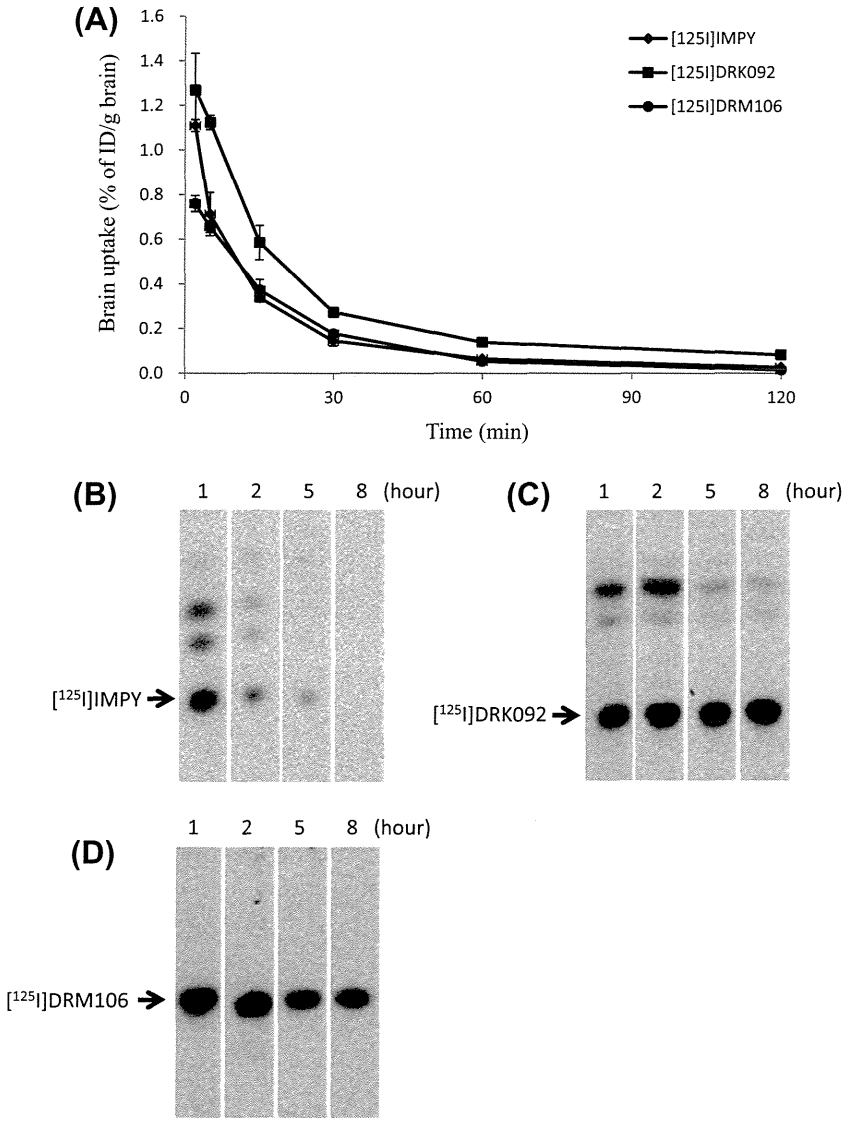

Figure 3. Brain uptake and metabolite production of radioligands in the normal rat brain. A: brain uptake of [^{125}I]IMPY (diamonds), [^{125}I]DRK092 (squares), and [^{125}I]DRM106 (circles); $n = 4$ for each experiment. B–C: brain samples were collected at the indicated time points after intravenous injection of [^{125}I]IMPY (B), [^{125}I]DRK092 (C), and [^{125}I]DRM106 (D); the metabolite production was analyzed with TLC as described in the Section 4.

pressure gave a residue, which was then purified by chromatography on a silica gel column using CH_2Cl_2/MeOH (95:5, v/v) to give **3** (1.03 g, 81%) as a colorless powder; ^{1}H NMR (400 MHz, DMSO-d_6) δ 7.47 (2H, d, J = 1.2 Hz), 7.98 (2H, d, J = 8.3 Hz), 8.18 (2H, d, J = 8.3 Hz), 8.49 (1H, s), 8.95 (1H, t, J = 1.2 Hz), 10.02 (1H, s).

4.1.4. 5-[4-(6-Iodoimidazo[1,2-*a*]pyridin-2-yl)phenyl]-1,3-oxazole (DRK092)

A mixture of **3** (647 mg, 1.86 mmol), K_2CO_3 (321 mg, 2.32 mmol) and *p*-toluenesulfonylmethylisocyanide (454 mg, 2.33 mmol) in MeOH (10 mL) was heated at reflux for 13 h. The precipitate was collected by filtration to give DRK092 (330 mg, 46%) as a colorless powder; mp: 284-286 °C. ^{1}H NMR (400 MHz, DMSO-d_6) δ 7.45 (2H, d, J = 1.2 Hz), 7.74 (1H, s), 7.81 (2H, d, J = 8.5 Hz), 8.06 (2H, d, J = 8.5 Hz), 8.39 (1H, s), 8.47 (1H, s), 8.92 (1H, t, J = 1.2 Hz). ^{13}C NMR (100 MHz, DMSO-d_6) δ 76.14, 109.37, 117.92, 122.12, 124.46, 126.22, 126.73, 131.46, 132.60, 133.51, 143.48, 143.87, 150.34, 151.83. HRMS (FAB) calcd for $C_{16}H_{11}IN_3O$ (M^+), 387.9947; found: 387.9905.

4.1.5. 4-(6-Iodoimidazo[1,2-*a*]pyridin-2-yl)-1-benzenecarbothioamide (4)

Thioacetamide (150 mg, 2.0 mmol) and **2** (345 mg, 1.0 mmol) were added to a solution of saturated hydrogen chloride in DMF (5 mL) and the reaction mixture was stirred at 80 °C for 4 h. After solvent removal under reduced pressure, aqueous saturated $NaHCO_3$ was added to the residue. The resulting precipitate was collected by filtration to give **4** (269 mg, 71%) as a colorless powder; ^{1}H NMR (400 MHz, DMSO-d_6) δ 7.45 (2H, d, J = 1.0 Hz), 7.98 (4H, s), 8.41 (1H, s), 8.92 (1H, s), 9.52 (1H, s), 9.86 (1H, s). FAB–MS m/z: 380 (M^++H).

4.1.6. 2-[4-(6-Iodoimidazo[1,2-*a*]pyridin-2-yl)phenyl]-1,3-thiazole (DRM101)

40% (w/w) chloroacetaldehyde in water (155 μL, 0.95 mmol) and Et_3N (91 μL, 0.65 mmol) were added to a solution of **4** (249 mg, 0.66 mmol) in EtOH (10 mL) and heated at reflux for 18 h. The reaction mixture was quenched with water and extracted with CH_2Cl_2/MeOH. The organic layer was washed with water, dried over Na_2SO_4, and evaporated under reduced pressure. The

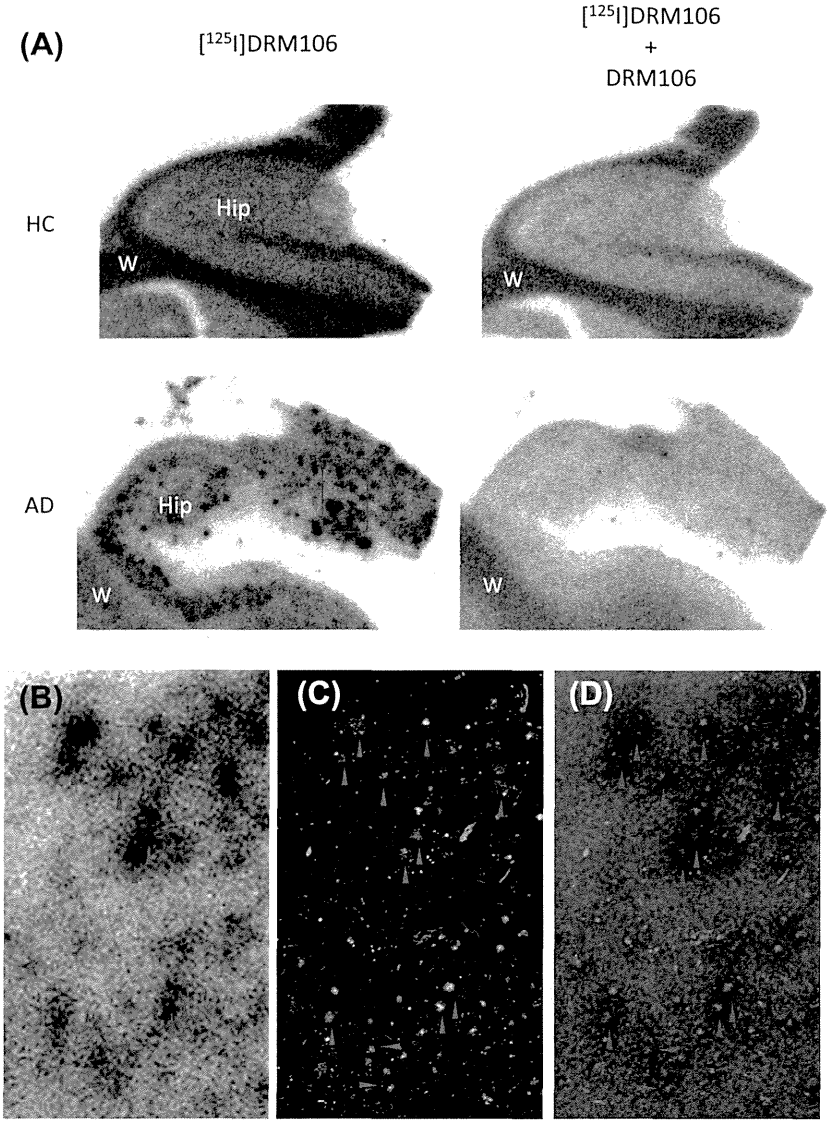

Figure 4. Amyloidosis-associated labeling of [^{125}I]DRM106 in postmortem human brains. A: autoradiographic images of [^{125}I]DRM106, in the absence (left column) and presence (right column) of non-radiolabeled DRM106, showed total and non-specific bindings of [^{125}I]DRM106, respectively, in postmortem healthy control (HC) and the sections of AD brain containing hippocampal regions. The area outlined by the red line is shown in panels B–D. Hip: hippocampus, W: white matter. B–D: co-localization of [^{125}I]DRM106 accumulation (B) and counterstaining of plaques with FSB (C). A merged image is displayed in panel D. The same brain section was stained with FSB after autoradiography.

residue was purified by silica gel column chromatography (CH_2Cl_2/MeOH, 100/5, v/v) to give DRM101 (103 mg, 39%) as a colorless powder; mp: 240–241 °C. ^{1}H NMR (400 MHz, DMSO-d_6) δ 7.45 (2H, s), 7.80 (1H, dd, J = 0.7, 3.2 Hz), 7.94 (1H, dd, J = 0.7, 3.2 Hz), 8.02 (2H, d, J = 8.1 Hz), 8.08 (2H, d, J = 8.3 Hz), 8.41 (1H, s), 8.93 (1H, d, J = 1.0 Hz). HRMS (FAB) calcd for $C_{16}H_{11}IN_3S$ (M^+), 403.9718; found: 403.9739.

4.1.7. *N*-Hydroxy-4-(6-iodoimidazo[1,2-*a*]pyridin-2-yl)benzamidine (5)

Hydroxylamine hydrochloride (208 mg, 3.0 mmol) and potassium carbonate (415 mg, 3.0 mmol) were added to a solution of **2** (345 mg, 1.0 mmol) in MeOH (10 mL). The reaction mixture was heated at reflux for 14 h. After the reaction mixture was cooled to room temperature, the resulting precipitate was collected by filtration and washed with water to give **5** (279 mg, 74%) as a pale yellow powder; ^{1}H NMR (400 MHz, DMSO-d_6) δ 5.82 (2H, s), 7.43 (2H, s), 7.74 (2H, d, J = 8.3 Hz), 7.94 (2H, d, J = 8.3 Hz), 8.34 (1H, s), 8.91 (1H, s), 9.65 (1H, s). EI-MS m/z: 378 (M^+).

4.1.8. 3-[4-(6-Iodoimidazo[1,2-*a*]pyridin-2-yl)]-1,2,4-oxadiazole (DRM102)

A mixture of **5** (265 mg, 0.70 mmol) and trimethylorthoformate (2.3 mL, 21.0 mmol) was heated at reflux for 18 h. After the reaction mixture was cooled at room temperature, the solvent was removed under reduced pressure and then CH_2Cl_2/MeOH was added. The resulting precipitate was collected by filtration to give DRM102 (217 mg, 80%) as a yellow powder; mp: 230–232 °C. ^{1}H NMR (400 MHz, DMSO-d_6) δ 7.46 (2H, s), 8.11 (2H, d, J = 8.3 Hz), 8.16 (2H, d, J = 8.3 Hz), 8.44 (1H, s), 8.94 (1H, d, J = 1.0 Hz), 9.71 (1H, d, J = 0.5 Hz). HRMS (FAB) calcd for $C_{15}H_{10}IN_4O$ (M^+), 388.9899; found: 388.9901.

4.1.9. 1-[4-(6-Iodoimidazo[1,2-*a*]pyridin-2-yl)phenyl]-1-ethanol (6)

Methyl magnesium bromide in diethyl ether (787 μL, 3.0 M, 2.36 mmol) was added dropwise to a solution of **3** (820 mg, 2.36 mmol) in THF (25 mL) at 0 °C under a nitrogen atmosphere. The reaction mixture was stirred at 0 °C for 15 min and then at

room temperature for 5 h. After being quenched with aqueous saturated ammonium chloride (25 mL) and stirred at room temperature for 1 h, the reaction mixture was extracted with CH_2Cl_2/MeOH. The organic layer was washed with water, dried over Na_2SO_4, and concentrated under reduced pressure. The residue was purified by silica gel column chromatography (CH_2Cl_2/MeOH, 97/3, v/v) to give **6** (579 mg, 63%) as yellow crystals; ^{1}H NMR (400 MHz, $CDCl_3$) δ 1.53 (3H, d, J = 6.3 Hz), 4.93 (1H, q, J = 6.5 Hz), 7.32 (1H, dd, J = 1.7, 9.4 Hz), 7.41 (2H, d, J = 7.6 Hz), 7.44 (1H, s), 7.78 (1H, s), 7.89 (2H, d, J = 8.1 Hz), 8.37 (1H, s).

4.1.10. 1-[4-(6-Iodoimidazo[1,2-*a*]pyridin-2-yl)phenyl]-2-ethanone (7)

Manganese dioxide (691 mg, 7.95 mmol) was added to a solution of **6** (579 mg, 1.59 mmol) in $CHCl_3$ (50 mL); the reaction mixture was heated at reflux for 8 h. After the suspension was filtered through Celite, the filtrate was concentrated under reduced pressure. The residue was purified by silica gel column chromatography (CH_2Cl_2/MeOH, 95/5, v/v) to give **7** (371 mg, 64%) as pale yellow crystals; ^{1}H NMR (400 MHz, DMSO-d_6) δ 2.60 (3H, s), 7.46 (2H, s), 8.03 (2H, d, J = 8.3 Hz), 8.09 (2H, d, J = 8.3 Hz), 8.46 (1H, s), 8.93 (1H, s). EI–MS m/z: 362 (M^+).

4.1.11. (*E*)-3-(Dimethylamino)-1-[4-(6-iodoimidazo[1,2-*a*]pyridin-2-yl)phenyl]-2-propen-1-one (8)

Under an argon atmosphere, *N*,*N*-dimethylformamide dimethyl acetal (363 μL, 2.73 mmol) was added dropwise to a solution of **7** (495 mg, 1.37 mmol) in DMF (50 mL); the reaction mixture was heated at 150 °C for 16 h. After the reaction mixture was concentrated under reduced pressure and the residue was purified by silica gel column chromatography (CH_2Cl_2/MeOH, 97/3, v/v) to give **8** (274 mg, 48%) as yellow crystals; ^{1}H NMR (400 MHz, $CDCl_3$) δ 2.97 (3H, br), 3.16 (3H, br), 5.77 (1H, d, J = 12.4 Hz), 7.35 (1H, dd, J = 1.5, 10.9 Hz), 7.44 (1H, d, J = 9.3 Hz), 7.83 (1H, d, J = 12.4 Hz), 7.86 (1H, s), 7.98 (4H, d, J = 0.5 Hz), 8.40 (1H, s). EI-MS m/z: 386 (M^+).

4.1.12. 6-Iodo-2-[4-(1*H*-3-pyrazolyl)phenyl]imidazo[1,2-*a*]pyridine (DRM106)

Hydrazine monohydrate (100 μL, 2.06 mmol) was added dropwise to a solution of **8** (344 mg, 0.82 mmol) in EtOH (30 mL) and heated at reflux for 3 h. After the reaction mixture was cooled at room temperature, the resulting precipitate was collected by filtration to give DRM106 (290 mg, 92%) as a colorless powder; mp: >300 °C. ^{1}H NMR (400 MHz, DMSO-d_6) δ 6.75 (1H, d, J = 1.7 Hz), 7.44 (2H, t, J = 9.8 Hz), 7.79 (1H, br), 7.87 (2H, d, J = 8.0 Hz), 7.98 (2H, d, J = 8.0 Hz), 8.34 (1H, s), 8.91 (1H, s), 12.90 (1H, br). ^{13}C NMR (100 MHz, DMSO-d_6) δ 75.8, 101.8, 108.8, 117.8, 125.4, 125.9, 129.8, 131.3, 132.3, 133.4, 143.4, 144.5, 149.7. HRMS (FAB) calcd for $C_{16}H_{12}IN_4$ (M^+), 387.0107; found: 387.0117.

4.1.13. 5-{4-[6-(Tributylstannyl)imidazo[1,2-*a*]pyridin-2-yl]phenyl}-1,3-oxazole (DRM015)

A mixture of DRK092 (580 mg, 1.50 mmol), bis(tributyltin) (1.74 g, 3.0 mmol), and $Pd(PPh_3)_4$ (173 mg, 0.15 mmol) in 1,4-dioxane (30 mL) was heated at reflux for 14 h under an argon atmosphere. After the solvent was removed under reduced pressure, the residue was purified by silica gel column chromatography (CH_2Cl_2/EtOAc, 7/3, v/v) to give DRM015 (400 mg, 49%) as brown oil; ^{1}H NMR (400 MHz, DMSO-d_6) δ 0.89–0.93 (9H, m), 1.07-1.15 (6H, m), 1.31–1.39 (6H, m), 1.53–1.61 (6H, m), 7.18 (1H, d, J = 8.8 Hz), 7.39 (1H, s), 7.60 (1H, d, J = 8.8 Hz), 7.73 (2H, d, J = 8.3 Hz), 7.88 (1H, s), 7.93 (1H, s), 8.00 (1H, s), 8.03 (2H, d, J = 8.3 Hz). ESI-MS m/z: 552 (M^+).

4.1.14. 2-[4-(1*H*-3-Pyrazolyl)phenyl]-6-(tributylstannyl)imidazo[1,2-*a*]pyridine (9)

A mixture of DRM106 (500 mg, 1.30 mmol), bis(tributyltin) (1.51 g, 2.6 mmol), and $Pd(PPh_3)_4$ (150 mg, 0.13 mmol) in 1,4-dioxane (30 mL) was heated at reflux for 16 h under an argon atmosphere. After the solvent was removed under reduced pressure, the residue was purified by silica gel column chromatography (CH_2Cl_2/MeOH, 95/5, v/v) to give **9** (300 mg, 42%) as a yellow oil; ^{1}H NMR (400 MHz, $CDCl_3$) δ 0.89–0.92 (9H, m), 1.06–1.25 (6H, m), 1.31–1.40 (6H, m), 1.53–1.63 (6H, m), 6.67 (1H, d, J = 2.4 Hz), 7.17 (1H, d, J = 8.8 Hz), 7.61 (1H, d, J = 8.8 Hz), 7.64 (1H, d, J = 2.4 Hz), 7.83 (2H, d, J = 8.3 Hz), 7.88 (1H, s), 8.00 (1H, s), 8.03 (2H, d, J = 8.3 Hz).

4.1.15. 2-{4-[1-(*tert*-Butoxycarbonyl)-3-pyrazoyl]phenyl}-6-(tributylstannyl)-imidazo[1,2-*a*]pyridine (DRN059)

Di-*tert*-butyl dicarbonate (1.1 mL, 4.79 mmol) was added to a solution of **9** (113 mg, 0.21 mmol) and dimethylaminopyridine (26 mg, 0.21 mmol) in CH_2Cl_2 (3 mL) at 0 °C. The reaction mixture was then stirred at room temperature for 8 h. This mixture was quenched with water and extracted with CH_2Cl_2. The organic layer was washed with water and saturated saline, dried over Na_2SO_4 and evaporated under reduced pressure. The residue was purified by silica gel chromatography (CH_2Cl_2/MeOH, 97/3, v/v) and produced DRN059 (127 mg, 93%) as colorless crystals; ^{1}H NMR (400 MHz, $CDCl_3$) δ 0.91 (9H, t, J = 7.3 Hz), 1.06–1.26 (6H, m), 1.31–1.40 (6H, m), 1.47–1.61 (6H, m), 1.68 (9H, s), 6.76 (1H, d, J = 2.9 Hz), 7.16 (1H, d, J = 8.8 Hz), 7.61 (1H, d, J = 8.5 Hz), 7.89 (1H, s), 7.98–8.04 (5H, m), 8.11 (1H, d, J = 3.0 Hz). FAB–MS m/z: 651 (M^++H).

4.2. Radiosynthesis

4.2.1. 6-[^{125}I]Iodo-2-[4-(1*H*-3-pyrazolyl)phenyl]imidazo[1,2-*a*]pyridine (DRM106)

Chloramine T (20 μL, 0.25 mg/mL) was added to a mixture of DRN059 (20 μL, 1 mg/mL in 2-propanol), sodium phosphate buffer (70 μL, 0.3 M, pH 5.5), and Na[^{125}I] (300 MBq, Nordion International, Ltd., Ottawa, ON, Canada) in a glass vial. The reaction was allowed to proceed for 5 min at room temperature; after this time, it was quenched by addition of 10 μL of a solution of NaOH (12 N). Subsequently, 100 μL of ethanol were added into the reaction vial and the reaction mixture was heated at 75 °C for 35 min, followed by cooling for 5 min. The reaction mixture was purified by HPLC, using a Capcellpak C_{18} UG-120 column (6.0 × 150 mm; Shiseido, Tokyo, Japan) with a mobile phase (EtOH/H_2O, 45/55, v/v) at a flow rate of 1.0 mL/min. Eluent volumes were diluted with a 4-fold volume of 20% EtOH, then loaded onto and passed through a pre-conditioned C_{18} Sep-Pak light cartridge (Waters Corporation; Milford, MA). After the cartridge was washed with distilled water (5 mL) and absolute EtOH (150 μL), [^{125}I]DRK092 was eluted by additional absolute EtOH (1 mL); ascorbic acid (final concentration: 5 mM) was added as a stabilizer to prevent oxidation and deiodination. The final product [^{125}I]DRM106 was obtained by filtration with a 0.20-μm filter. Its radiochemical purity was analyzed by TLC. [^{125}I]DRM106 was applied to TLC plates (Whatman KC-18F) and eluted with an elution buffer, that is, MeOH/H_2O/NH_3 = 80/19/1. Radioactivity of separated spots was quantified by autoradiography. The specific activity and the radiochemical purity were determined to be 81.4 GBq/μmol and >95%, respectively. The solution was stored at −20 °C until used.

4.2.2. 5-[4-(6-[^{125}I]Iodoimidazo[1,2-*a*]pyridine-2-yl)phenyl]-1,3-oxazole (DRK092)

Chloramine T (20 μL, 0.10 mg/mL) was added to a mixture of DRM015 (20 μL, 1 mg/mL in EtOH), sodium phosphate buffer

(70 μL, 0.3 M, pH 5.5), and Na[^{125}I] (300 MBq) in a glass vial. After the reaction was allowed to proceed for 2 min at room temperature, the reaction was quenched with aqueous sodium metabisulfite (100 μL, 2.0 mg/mL). The reaction mixture was purified following a protocol similar to that employed for [^{125}I]DRM106; however, a modified mobile phase (MeOH/H_2O, 60/40, v/v) for HPLC was used. The specific activity and the radiochemical purity were determined to be 81.4 GBq/μmol and >95%, respectively. The solution was stored at −20 °C until used.

4.3. Binding assay for IC_{50} estimation

Lyophilized synthetic Aβ1-40 was purchased from Peptide Institute Inc. (Osaka, Japan). Aβ fibrils were generated by spontaneous assembly. Aβ1-40 peptides (final concentration: 100 nM) were dissolved in 10 mM potassium phosphate buffered saline (PBS, pH7.4) containing 1 mM EDTA and incubated at 37 °C for 4 days with gentle and constant shaking. Aggregated Aβ fibrils were stored at 4 °C until used.

The 100-μL aliquots of synthetic human Aβ (1–40) fibrils were combined with 900 μL of PBS containing [^{125}I]IMPY (0.1 nM), 1% EtOH, and 20 mM ascorbic acid in the presence of compounds with a concentration ranging from 0.04 to 1000 nM. The reaction mixture was incubated at 37 °C for 3 h, followed by vacuum filtration through Whatman GF/B filters using a Brandel cell harvester (Model M-24R, Biomedical Research. Lab., Gaithesburg, MD). The GF/B filters were counted by gamma counter after three rapid washes with 2 mL of ice-cold PBS containing 0.1 mM ascorbic acid. No and full inhibitory effects were measured with the addition of vehicle and nonradiolabeled IMPY (500 nM), respectively. The IC_{50} was generated by Scatchard analysis using GraphPad Prism (GraphPad Software, version 4.0, San Diego, CA).

4.4. Log$D_{7.4}$ measurements

The experimental determination of the partition coefficients was performed according to a method previously published, which employs HPLC.[22,23] The compounds for the standard curve were analyzed by HPLC with the following conditions: symmetry C_{18} column (3.9 × 150 mm; Waters Corporation); mobile phase, for example, 20 mM 3-morpholinopropanesulfonic acid (pH 7.4) containing various methanol concentration (from 60% to 85%), flow rate (1.0 ml/min), UV wavelength (256 or 300 nm. The capacity factor at various methanol concentrations ($k_{\%}$) was calculated according to a method previously published[24], using the following equation: $k_{\%} = (t_{\%} - t_0)/t_0$, where $t_{\%}$ and t_0 are the retention times of the ligand and the non-retained peak, respectively. The logarithms of the capacity factors ($\log k_{\%}$) were plotted versus methanol concentrations; $\log k_w$ was obtained by linear extrapolation to 0% methanol concentration. The $\log D_{7.4}$ values of standard compounds were obtained from previously published data[22,23]; those of novel compounds were calculated in this work from the standard curve based on their log k_w values.

4.5. Biodistribution and metabolite analysis in normal rats

Normal Sprague-Dawley (SD) rats (8 weeks old) for biodistribution and metabolite analyses were purchased from Charles River Laboratories Japan Inc. (Yokohama, Japan). The rats were administered with radioligands (1.85 MBq/kg body weight for each ligand) via the tail vein, and euthanized by cervical dislocation under isoflurane anesthesia at designed time points. Radioactivity in the organs of interest was measured by gamma counter (Wallac Wizard 1480; PerkinElmer Wallac Inc, Turku, Finland). The uptake of radiolabeled ligands was expressed as a percentage of the injected dose per gram of tissue (% of ID/g tissue), except for the thyroid uptake, which was expressed as percentage of the injected dose (% of ID).

In order to carry out the metabolite analysis, the brain samples were collected at specific times in additional experiments. In particular, the collected brain tissues were homogenized in 2-fold volume of saline, containing 0.1% between 80 and 40 mM sodium L-ascorbate. 50-μL aliquots of samples were then added to the same volumes of acetonitrile, and the mixtures were applied to a Mini-UniPrep (UN203NPUORG 0.45 μm, GE Healthcare Bio-Sciences, Piscataway Township, NJ), followed by filtration to remove the denatured proteins. The filtrates were applied to TLC plates and eluted by 80% ethanol in water. Radioactivity of separated spots was quantified by autoradiography.

4.6. In vitro autoradiographic analysis

Postmortem human brains for in vitro autoradiographic analysis were obtained from the Center for Neurodegenerative Disease Research at the University of Pennsylvania (Perelman School of Medicine), from patients with AD. Deparaffinized brain sections (thickness of 10 μm) were preincubated with a blocking solution (1% BSA, 4% ethanol, 40 mM sodium L-ascorbate in PBS) for 30 min, and then incubated with [^{125}I]DRM106 (0.5 nM) at room temperature for 3 h, with/without non-radiolabeled DRM106 (10 μM). The brain sections were then dipped in PBS for 10 s and rinsed with 20% ethanol for 1 min, followed by rinsing with PBS six times, for 5 min each, and finally dipped into distilled water for 10 s. The brain sections were blow-dried with warm air and attached to imaging plates (BAS-MS2025; Fujifilm, Tokyo, Japan) overnight. Radiolabeling was then detected by scanning the imaging plate, using the BAS5000 system (Fujifilm) or Typhoon FLA 7000 scanner system (GE Healthcare). The same brain sections were used for counterstaining of plaques with 0.01% (*E,E*)-1-fluoro-2,5-bis(3-hydroxycarbony-4-hydroxy)styrylbenzene (FSB; Dojindo Laboratories, Kumamoto, Japan) as described in our previous study.[2]

Acknowledgments

The authors thank Prof. John Q. Trojanowski and Prof. Virginia M.-Y. Lee (Center for Neurodegenerative Disease Research, University of Pennsylvania) for kindly providing human tissue. This work was supported in part by Grants-in-Aid for Japan Advanced Molecular Imaging Program and Core Research for Evolutional Science and Technology (T.S.), and Scientific Research on Innovative Areas ('Brain Environment') 23111009 (M.H.) from the Ministry of Education, Culture, Sports, Science and Technology, Japan.

Supplementary data

Supplementary data associated with this article can be found, in the online version, at http://dx.doi.org/10.1016/j.bmc.2014.05.043.

References and notes

1. Braak, H.; Braak, E. *Acta Neuropathol. (Berl)* **1991**, *82*, 239.
2. Maeda, J.; Ji, B.; Irie, T.; Tomiyama, T.; Maruyama, M.; Okauchi, T.; Staufenbiel, M.; Iwata, N.; Ono, M.; Saido, T. C.; Suzuki, K.; Mori, H.; Higuchi, M.; Suhara, T. *J. Neurosci.* **2007**, *27*, 10957.
3. Klunk, W. E.; Engler, H.; Nordberg, A.; Wang, Y.; Blomqvist, G.; Holt, D. P.; Bergstrom, M.; Savitcheva, I.; Huang, G. F.; Estrada, S.; Ausen, B.; Debnath, M. L.; Barletta, J.; Price, J. C.; Sandell, J.; Lopresti, B. J.; Wall, A.; Koivisto, P.; Antoni, G.; Mathis, C. A.; Langstrom, B. *Ann. Neurol.* **2004**, *55*, 306.
4. Camus, V.; Payoux, P.; Barre, L.; Desgranges, B.; Voisin, T.; Tauber, C.; La Joie, R.; Tafani, M.; Hommet, C.; Chetelat, G.; Mondon, K.; de La Sayette, V.; Cottier, J. P.; Beaufils, E.; Ribeiro, M. J.; Gissot, V.; Vierron, E.; Vercouillie, J.; Vellas, B.; Eustache, F.; Guilloteau, D. *Eur. J. Nucl. Med. Mol. Imaging* **2012**, *39*, 621.
5. Cselenyi, Z.; Jonhagen, M. E.; Forsberg, A.; Halldin, C.; Julin, P.; Schou, M.; Johnstrom, P.; Varnas, K.; Svensson, S.; Farde, L. *J. Nucl. Med.* **2012**, *53*, 415.

6. Engler, H.; Forsberg, A.; Almkvist, O.; Blomquist, G.; Larsson, E.; Savitcheva, I.; Wall, A.; Ringheim, A.; Langstrom, B.; Nordberg, A. *Brain* **2006**, *129*, 2856.
7. Ikonomovic, M. D.; Klunk, W. E.; Abrahamson, E. E.; Mathis, C. A.; Price, J. C.; Tsopelas, N. D.; Lopresti, B. J.; Ziolko, S.; Bi, W.; Paljug, W. R.; Debnath, M. L.; Hope, C. E.; Isanski, B. A.; Hamilton, R. L.; DeKosky, S. T. *Brain* **2008**, *131*, 1630.
8. Leinonen, V.; Alafuzoff, I.; Aalto, S.; Suotunen, T.; Savolainen, S.; Nagren, K.; Tapiola, T.; Pirttila, T.; Rinne, J.; Jaaskelainen, J. E.; Soininen, H.; Rinne, J. O. *Arch. Neurol.* **2008**, *65*, 1304.
9. Okello, A.; Koivunen, J.; Edison, P.; Archer, H. A.; Turkheimer, F. E.; Nagren, K.; Bullock, R.; Walker, Z.; Kennedy, A.; Fox, N. C.; Rossor, M. N.; Rinne, J. O.; Brooks, D. J. *Neurology* **2009**, *73*, 754.
10. Zhang, W.; Kung, M. P.; Oya, S.; Hou, C.; Kung, H. F. *Nucl. Med. Biol.* **2007**, *34*, 89.
11. Choi, S. R.; Golding, G.; Zhuang, Z.; Zhang, W.; Lim, N.; Hefti, F.; Benedum, T. E.; Kilbourn, M. R.; Skovronsky, D.; Kung, H. F. *J. Nucl. Med.* **1887**, *2009*, 50.
12. Hampel, H.; Wilcock, G.; Andrieu, S.; Aisen, P.; Blennow, K.; Broich, K.; Carrillo, M.; Fox, N. C.; Frisoni, G. B.; Isaac, M.; Lovestone, S.; Nordberg, A.; Prvulovic, D.; Sampaio, C.; Scheltens, P.; Weiner, M.; Winblad, B.; Coley, N.; Vellas, B. *Prog. Neurobiol.* **2011**, *95*, 579.
13. Watanabe, H.; Ono, M.; Ikeoka, R.; Haratake, M.; Saji, H.; Nakayama, M. *Bioorg. Med. Chem.* **2009**, *17*, 6402.
14. Maya, Y.; Ono, M.; Watanabe, H.; Haratake, M.; Saji, H.; Nakayama, M. *Bioconjugate Chem.* **2009**, *20*, 95.
15. Qu, W.; Kung, M. P.; Hou, C.; Oya, S.; Kung, H. F. *J. Med. Chem.* **2007**, *50*, 3380.
16. Ono, M.; Cheng, Y.; Kimura, H.; Watanabe, H.; Matsumura, K.; Yoshimura, M.; Iikuni, S.; Okamoto, Y.; Ihara, M.; Takahashi, R.; Saji, H. *PLoS ONE* **2013**, *8*, e74104.
17. Zhuang, Z. P.; Kung, M. P.; Wilson, A.; Lee, C. W.; Plossl, K.; Hou, C.; Holtzman, D. M.; Kung, H. F. *J. Med. Chem.* **2003**, *46*, 237.
18. Newberg, A. B.; Wintering, N. A.; Plossl, K.; Hochold, J.; Stabin, M. G.; Watson, M.; Skovronsky, D.; Clark, C. M.; Kung, M. P.; Kung, H. F. *J. Nucl. Med.* **2006**, *47*, 748.
19. Kung, M. P.; Hou, C.; Zhuang, Z. P.; Zhang, B.; Skovronsky, D.; Trojanowski, J. Q.; Lee, V. M.; Kung, H. F. *Brain Res.* **2002**, *956*, 202.
20. Kung, M. P.; Hou, C.; Zhuang, Z. P.; Cross, A. J.; Maier, D. L.; Kung, H. F. *Eur. J. Nucl. Med. Mol. Imaging* **2004**, *31*, 1136.
21. Kung, M. P.; Weng, C. C.; Lin, K. J.; Hsiao, I. T.; Yen, T. C.; Wey, S. P. *Chang Gung Med. J.* **2012**, *35*, 211.
22. Kerns, E. H.; Di, L.; Petusky, S.; Kleintop, T.; Huryn, D.; McConnell, O.; Carter, G. *J. Chromatogr. B* **2003**, *791*, 381.
23. Lombardo, F.; Shalaeva, M. Y.; Tupper, K. A.; Gao, F. *J. Med. Chem.* **2001**, *44*, 2490.
24. Kessler, R. M.; Ansari, M. S.; de Paulis, T.; Schmidt, D. E.; Clanton, J. A.; Smith, H. E.; Manning, R. G.; Gillespie, D.; Ebert, M. H. *J. Nucl. Med.* **1991**, *32*, 1593.

JNM The Journal of NUCLEAR MEDICINE

Quantitative Analysis of Amyloid Deposition in Alzheimer Disease Using PET and the Radiotracer ^{11}C-AZD2184

Hiroshi Ito, Hitoshi Shimada, Hitoshi Shinotoh, Harumasa Takano, Takeshi Sasaki, Tsuyoshi Nogami, Masayuki Suzuki, Tomohisa Nagashima, Keisuke Takahata, Chie Seki, Fumitoshi Kodaka, Yoko Eguchi, Hironobu Fujiwara, Yasuyuki Kimura, Shigeki Hirano, Yoko Ikoma, Makoto Higuchi, Kazunori Kawamura, Toshimitsu Fukumura, Éva Lindström Böö, Lars Farde and Tetsuya Suhara

J Nucl Med. 2014;55:932-938.
Published online: April 14, 2014.
Doi: 10.2967/jnumed.113.133793

The Journal of Nuclear Medicine is published monthly.
SNMMI | Society of Nuclear Medicine and Molecular Imaging
1850 Samuel Morse Drive, Reston, VA 20190.
(Print ISSN: 0161-5505, Online ISSN: 2159-662X)

SNMMI SOCIETY OF NUCLEAR MEDICINE AND MOLECULAR IMAGING

Quantitative Analysis of Amyloid Deposition in Alzheimer Disease Using PET and the Radiotracer ^{11}C-AZD2184

Hiroshi Ito[1], Hitoshi Shimada[1], Hitoshi Shinotoh[1], Harumasa Takano[1], Takeshi Sasaki[1], Tsuyoshi Nogami[1], Masayuki Suzuki[1], Tomohisa Nagashima[1], Keisuke Takahata[1], Chie Seki[1], Fumitoshi Kodaka[1], Yoko Eguchi[1], Hironobu Fujiwara[1], Yasuyuki Kimura[1], Shigeki Hirano[1], Yoko Ikoma[1], Makoto Higuchi[1], Kazunori Kawamura[1], Toshimitsu Fukumura[1], Éva Lindström Böö[2], Lars Farde[2], and Tetsuya Suhara[1]

[1]*Molecular Imaging Center, National Institute of Radiological Sciences, Chiba, Japan; and* [2]*AstraZeneca Translational Sciences Center, Department of Clinical Neuroscience, Karolinska Institutet, Stockholm, Sweden*

Characteristic neuropathologic changes in Alzheimer disease (AD) are amyloid-β deposits and neurofibrillary tangles. Recently, a new radioligand for amyloid senile plaques, ^{11}C-labeled 5-(6-{[tert-butyl(dimethyl)silyl]oxy}-1,3-benzothiazol-2-yl)pyridin-2-amine (^{11}C-AZD2184), was developed, and it was reported to show rapid brain uptake followed by rapid washout. In this study, ^{11}C-AZD2184 binding in control subjects and AD patients was examined in more detail by compartment model analysis using a metabolite-corrected arterial input function. The accuracy of simplified quantitative methods using a reference brain region was also evaluated. **Methods:** After intravenous bolus injection of ^{11}C-AZD2184, a dynamic PET scan was obtained for 90 min in 6 control subjects and 8 AD patients. To obtain the arterial input function, arterial blood sampling and high-performance liquid chromatography analysis were performed. **Results:** Time–activity curves in all brain regions could be described using the standard 2-tissue-compartment model. The total distribution volume ratios to reference region (*DVR*) in cerebral cortical regions were significantly higher in AD patients than in control subjects. Although there was no conspicuous accumulation of radioactivity in white matter as compared with other amyloid radioligands, *DVR* values in the centrum semiovale were more than 1 for both control subjects and AD patients, suggesting binding to myelin. The standardized uptake value ratio calculated from integrated time–activity curves in brain regions and the reference region was statistically in good agreement with *DVR*. **Conclusion:** Although the white matter binding of ^{11}C-AZD2184 may have some effect on cortical measurement, it can be concluded that the kinetic behavior of ^{11}C-AZD2184 is suitable for quantitative analysis. The standardized uptake value ratio can be used as a validated measure of ^{11}C-AZD2184 binding in clinical examinations without arterial input function.

Key Words: amyloid; Alzheimer; PET; AZD2184

J Nucl Med 2014; 55:932–938
DOI: 10.2967/jnumed.113.133793

Alzheimer disease (AD) is the most common neurodegenerative disorder. Characteristic neuropathologic changes in AD are amyloid-β deposits and neurofibrillary tangles (*1*). The amyloid cascade hypothesis states that the deposition of amyloid-β drives the remaining Alzheimer pathology, for example, formation of neurofibrillary tangles, cell loss, and vascular damage (*2*). From this perspective, in vivo imaging of amyloid-β deposits may contribute to early diagnosis of AD and serve as a marker for evaluation of disease-modifying drugs. To measure amyloid-β deposits by PET, several radiotracers, for example, ^{11}C-Pittsburgh compound B (^{11}C-PIB) (*3,4*) and (*E*)-4-(2-(6-(2-(2-(2-^{18}F-fluoroethoxy)ethoxy)ethoxy) pyridin-3-yl)vinyl)-*N*-methyl benzenamine (*5*), have been developed and used for examination of the pathophysiology of AD.

^{11}C-labeled 5-(6-{[tert-butyl(dimethyl)silyl]oxy}-1,3-benzothiazol-2-yl)pyridin-2-amine (^{11}C-AZD2184) is a more recently developed radiotracer for amyloid-β deposits. ^{11}C-AZD2184 has been characterized in preclinical studies and has high affinity in vitro for amyloid fibrils (dissociation constant, 8.4 ± 1.0 nM) (*6*). After intravenous injection of ^{11}C-AZD2184 in an initial human study, there was rapid uptake of radioactivity in the brain, followed by rapid washout in control subjects and in AD patients (*7*). The ratios of uptake in cortical regions to a reference brain region devoid of amyloid-β deposition were close to unity in control subjects and high in AD patients. In addition, there was no conspicuous accumulation of radioactivity in white matter.

The initial results indicate that ^{11}C-AZD2184 has potential as a sensitive imaging biomarker for research on the pathophysiology and treatment of AD. The aim of the present study was to examine ^{11}C-AZD2184 binding in greater detail by compartment model analysis using a metabolite-corrected arterial input function. The accuracy of simplified quantitative methods using a reference brain region was also evaluated.

MATERIALS AND METHODS

Subjects

Six control subjects (mean age ± SD, 65 ± 10 y) and 8 AD patients (72 ± 12 y) were recruited (Table 1). All AD patients were diagnosed according to the criteria of the National Institute of Neurologic and Communicative Diseases and Stroke/Alzheimer Disease and Related Disorders Association (*8*). All subjects were characterized according to the Clinical Dementia Rating scale (*9*). The control subjects were rated as 0 by the Clinical Dementia Rating scale, whereas the AD subjects were rated as 0.5, 1, or 2. In addition, the Mini-Mental State Examination was performed in

Received Oct. 10, 2013; revision accepted Jan. 27, 2013.
For correspondence or reprints contact: Hiroshi Ito, Biophysics Program, Molecular Imaging Center, National Institute of Radiological Sciences, 4-9-1 Anagawa, Inage-ku, Chiba 263-8555, Japan.
E-mail: hito@nirs.go.jp
Published online Apr. 14, 2014.

TABLE 1
Profiles of Subjects

Subject group	Subject no.	Age (y)	Sex	Mini-Mental State Examination score	Clinical Dementia Rating scale
Control	NC1	61	F	28	0
	NC2	51	M	29	0
	NC3	60	M	30	0
	NC4	74	M	29	0
	NC5	71	M	28	0
	NC6	75	F	29	0
AD	AD1	76	F	15	1
	AD2	55	F	24	1
	AD3	63	M	13	1
	AD4	75	M	20	0.5
	AD5	84	F	13	1
	AD6	82	F	23	0.5
	AD7	82	F	19	1
	AD8	58	M	13	1

all subjects (*10*). No subject had any observable organic brain lesion according to MR imaging. Control subjects had no cognitive impairment and were free from medications for the central nervous system. The study was approved by the Institutional Review Board of the National Institute of Radiologic Sciences, Chiba, Japan. Written informed consent was obtained from all subjects or from their spouses or other close family members.

Radioligand

^{11}C-AZD2184 was produced according to the literature (*11*). In brief, ^{11}C-AZD2184 was radiosynthesized by reaction of the precursor 5-(6-(tert-butyldimethyl-silyloxy)benzo[d]thiazol-2-yl)pyridin-2-amine with ^{11}C-CH_3I in the presence of potassium hydroxide and subsequent deprotection by water (*7*).

PET Experimental Procedure

All PET measurements were performed with a SET-3000GCT/X scanner (Shimadzu Corp.) (*12*), which provides 99 sections with an axial field of view of 26 cm. The intrinsic spatial resolution is 3.4 mm in-plane and 5.0 mm in full width at half maximum axially. Images were reconstructed by the filtered backprojection algorithm. With a gaussian filter (cutoff frequency, 0.3 cycle/pixel), the reconstructed in-plane resolution was 7.5 mm in full width at half maximum. Data were acquired in 3-dimensional mode. Scatter correction was done by a hybrid scatter-correction method based on acquisition with dual-energy window setting (*13*). A 4-min transmission scan using a ^{137}Cs line source was obtained to correct for attenuation.

After intravenous bolus injection of ^{11}C-AZD2184 over 1 min, a dynamic PET scan was obtained for 90 min. The frame sequence consisted of six 10-s, three 20-s, six 1-min, four 3-min, and fourteen 5-min frames. The radioactivity injected was 380 ± 12 and 380 ± 13 MBq, and the specific radioactivity was 131 ± 38 and 119 ± 28 GBq/μmol at the time of injection for control subjects and AD patients, respectively.

To obtain the arterial input function, 32 samples of arterial blood were taken after injection. The fraction of radioactivity representing unchanged ^{11}C-AZD2184 in plasma was determined by high-performance

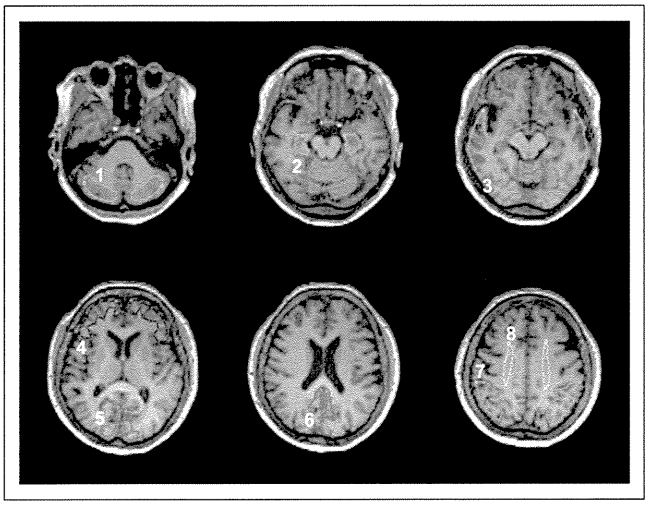

FIGURE 1. ROIs drawn on coregistered MR images. ROIs are defined for cerebellar cortex (1), parahippocampal gyrus including hippocampus (2), lateral side of temporal cortex (3), base side of frontal cortex (4), cuneus of occipital cortex (5), posterior region of cingulate gyrus (6), parietal cortex (7), and centrum semiovale (8).

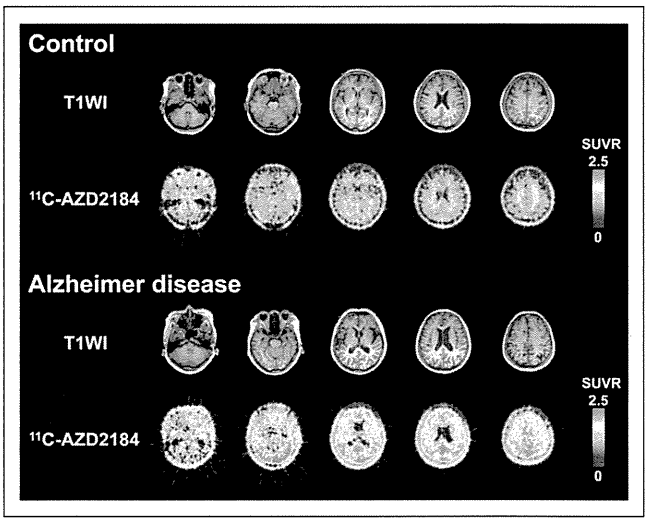

FIGURE 2. Representative *SUVR* images of ^{11}C-AZD2184 binding in control subject and AD patient. Integration interval was 40–60 min. Corresponding MR images (T1-weighted [T1WI]) are shown. Scale maximum and minimum values are 2.5 and 0 of *SUVR*. All images are transaxial sections, and anterior is at top of image and subjects' right is at left.

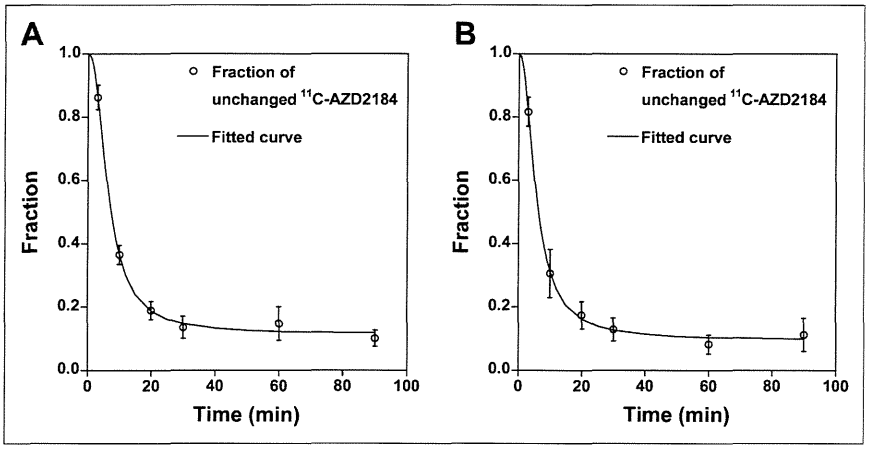

FIGURE 3. Time courses of fraction of radioactivity representing unchanged ^{11}C-AZD2184 in plasma for control subjects (A) and AD patients (B). Values are mean ± SD. Fitted curves were obtained using Hill equation.

liquid chromatography from 6 blood samples for each subject. Acetonitrile was added to each plasma sample, and the samples were then centrifuged. The obtained supernatant was subjected to radio–high-performance liquid chromatography analysis (column, μBondapak [10 μm, 7.8 × 300 nm]; Waters) (mobile phase, 90% acetonitrile [A]/1 mol/L ammonium formate [B]; gradient, 0–10 min [A/B], 22/78–47/53, 10–11 min [A/B], 47/53–80/20, and 11–12 min [A/B], 80/20–22/78; isocratic, 12–15 min end; flow rate, 6.0 mL/min). Plasma protein binding was not determined in the present study. The time curves for the fraction of unchanged ^{11}C-AZD2184 in plasma were fitted by the Hill equation and used for kinetic analysis.

MR Imaging Procedure

All MR imaging examinations were performed with a 3-T MR scanner (GE Healthcare). Three-dimensional volumetric acquisition of a T1-weighted 3-dimensional fast spoiled gradient-recalled acquisition in the steady-state sequence produced a gapless series of thin transverse sections (echo time, 2.848 ms; repetition time, 6.992 ms; prep time, 900 ms; flip angle, 8°; field of view, 260 mm; acquisition matrix, 256 × 256; slice thickness, 1 mm; scan time, 367 s). Proton density–weighted and T2-weighted images were obtained by a 2-dimensional double-echo fast spin echo sequence with interleaved and gapless acquisition (echo time for proton density–weighted images, 10.58 ms; effective echo time for T2-weighted images, 95.22 ms; repetition time, 3,000.00 ms; field of view, 240 mm; acquisition matrix, 256 × 256; slice thickness, 3 mm [no gap, interleave]; echo train length, 16; scan time, 309 s). T1-weighted images were used for analysis of PET images. Proton density–weighted and T2-weighted images were used to confirm whether subjects had any observable organic brain lesion.

Regions of Interest (ROIs)

All MR images were coregistered to the individual PET images using the software package PMOD (version 3.0; PMOD Technologies Ltd.). ROIs were drawn on coregistered MR images (T1-weighted images) and transferred to the PET images. ROIs were defined for the cerebellar cortex, parahippocampal gyrus including the hippocampus, posterior region of the cingulate gyrus, base side of the frontal cortex, lateral side of the temporal cortex, parietal cortex, cuneus of the occipital cortex, and centrum semiovale (Fig. 1). Each ROI was drawn on 3 adjacent sections, and data were pooled to obtain the average radioactivity concentration for the whole volume of interest. To obtain regional time–activity curves, regional radioactivity was calculated for each frame, corrected for decay, and plotted versus time.

Kinetic Model for Interpretation of ^{11}C-AZD2184 Binding

To interpret the kinetic behavior of ^{11}C-AZD2184, the standard 2-tissue-compartment model with 4 first-order rate constants was used (*14*). The rate constants K_1 and k_2 describe the influx and efflux rates for radiotracer diffusion through the blood–brain barrier, respectively. The rate constants k_3 and k_4 describe the radiotracer transfer between the compartments for nondisplaceable radiotracer and specific binding. The distribution volume with only nondisplaceable binding in a brain region (V_{ND}), the total distribution volume (V_T), and the binding potential relative to the concentration of nondisplaceable radiotracer in brain (BP_{ND}) are expressed as follows (*15*):

$$V_{ND} = \frac{K_1}{k_2} \quad \text{Eq. 1}$$

$$V_T = \frac{K_1}{k_2}\left(1 + \frac{k_3}{k_4}\right) \quad \text{Eq. 2}$$

$$BP_{ND} = \frac{k_3}{k_4} \quad \text{Eq. 3}$$

Kinetic Analysis of ^{11}C-AZD2184 Binding

To estimate the rate constants (K_1, k_2, k_3, and k_4), nonlinear curve fitting was performed in a least-squares sense to the regional time–activity curves (*16*). In this analysis, the blood volume, which depends on the first-pass extraction fraction of the tracer, was assumed to be 0.04 mL/mL to diminish the influence of tracer remaining in the blood using the radioactivity of whole blood (*17*). The radioactivity of unchanged ^{11}C-AZD2184

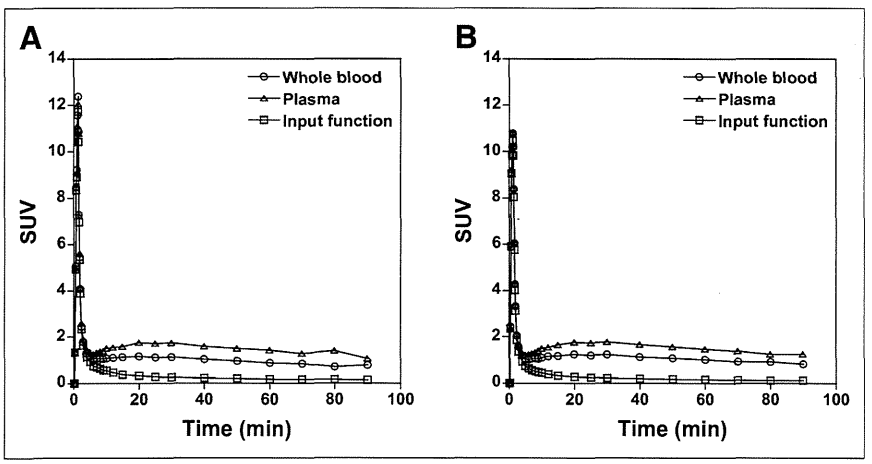

FIGURE 4. Time courses of average radioactivity concentration in arterial whole blood and plasma for control subjects (A) and AD patients (B). Time courses of average radioactivity concentration of unchanged ^{11}C-AZD2184 in plasma (i.e., arterial input function) are also shown.

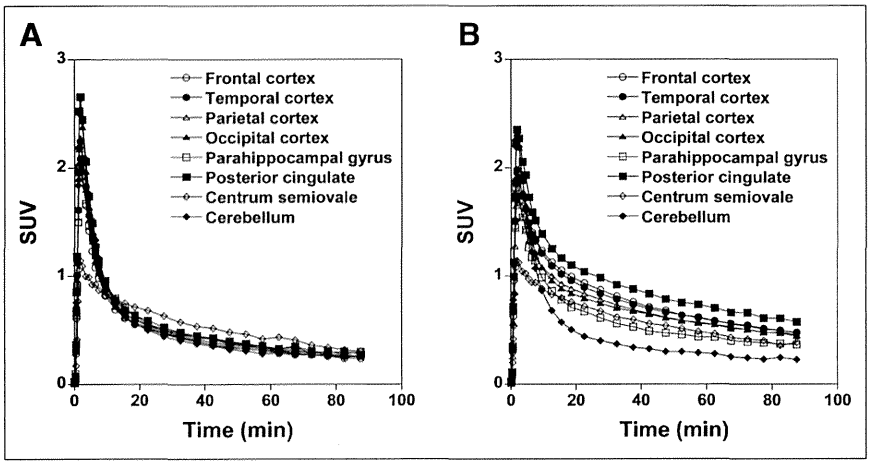

FIGURE 5. Average time–activity curves for brain regions in control subjects (A) and AD patients (B).

in plasma was used as the arterial input function. For this analysis, PMOD was used. V_T was calculated from the rate constants as an indicator of amyloid-β deposits (Eq. 2).

Quantitative Approach Using Reference Region

The cerebellum has been suggested as a reference brain region because no fibrillar amyloid plaques have been demonstrated in this region postmortem (*18,19*). A quantitative approach, taking advantage of the cerebellum as a reference region, can be used to calculate the total distribution volume ratio (*DVR*) as follows:

$$DVR = V_{T(brain)}/V_{T(cerebellum)}, \quad \text{Eq. 4}$$

where $V_{T(brain)}$ and $V_{T(cerebellum)}$ are total distribution volume in brain regions and the cerebellum, respectively. The BP_{ND} is equal to *DVR* – 1 if the cerebellum is the ideal reference brain region.

In addition, the standardized uptake value (*SUV*) was calculated from the time-integrated regional radioactivity concentration normalized with injected dose per body weight. The integration intervals were 20–40, 40–60, and 60–90 min. The integration interval of 20–40 min includes the peak equilibrium condition (*20*), and the integration intervals of 40–60 and 60–90 min correspond to the late part of the time–activity curve. In a simplified approach and because the cerebellum can be used as a reference brain region, the *SUV* ratio (*SUVR*) indicating amyloid-β deposits was calculated using the following expression:

$$SUVR = SUV_{brain}/SUV_{cerebellum}, \quad \text{Eq. 5}$$

where SUV_{brain} and $SUV_{cerebellum}$ represent the *SUV* in brain regions and the cerebellum, respectively.

RESULTS

In this study, no adverse event was observed after intravenous injection of ^{11}C-AZD2184. Representative *SUVR* images showing the distribution of brain radioactivity after intravenous injection of ^{11}C-AZD2184 are shown for a control subject and an AD patient in Figure 2. There was no conspicuous accumulation of radioactivity in white matter, the same as in a previous report (*7*). In AD patients, radioactivity in the cerebral cortices was higher than in the control subjects. By visual assessment of the *SUVR* images, all control subjects appeared negative with regard to specific binding of ^{11}C-AZD2184, whereas all AD patients appeared positive.

The time courses for the average fraction of radioactivity representing unchanged ^{11}C-AZD2184 in plasma for control subjects and AD patients are shown in Figure 3. Sixty minutes after injection of ^{11}C-AZD2184, the fraction of radioactivity representing unchanged ^{11}C-AZD2184 in plasma was 0.11–0.12. The time courses of the average radioactivity concentration in whole blood and plasma and the time course of the radioactivity concentration of unchanged ^{11}C-AZD2184 in plasma (i.e., arterial input function) are shown in Figure 4.

The regional time–activity curves for control subjects and AD patients are shown in Figure 5. At 18.5, 37.5, 57.5, and 87.5 min after injection of ^{11}C-AZD2184, the ratios of regional radioactivity of posterior cingulate to cerebellum were 1.14 ± 0.03, 1.21 ± 0.09, 1.27 ± 0.17, and 1.08 ± 0.27 for control subjects and 2.19 ± 0.22, 2.60 ± 0.57, 2.55 ± 0.49, and 2.52 ± 0.64 for AD patients. In control subjects, radioactivity concentrations in cerebral cortical regions were similar to those for the cerebellum at the end of data acquisition, the same as in a previous report (*7*). In AD patients, radioactivity concentrations in cerebral cortical regions were higher than in the cerebellum.

Typical time–activity curves in brain regions of an AD patient and the corresponding fitted curves obtained by kinetic analyses are shown in Figure 6. The time–activity curves in all brain regions could be described by the standard 2-tissue-compartment model.

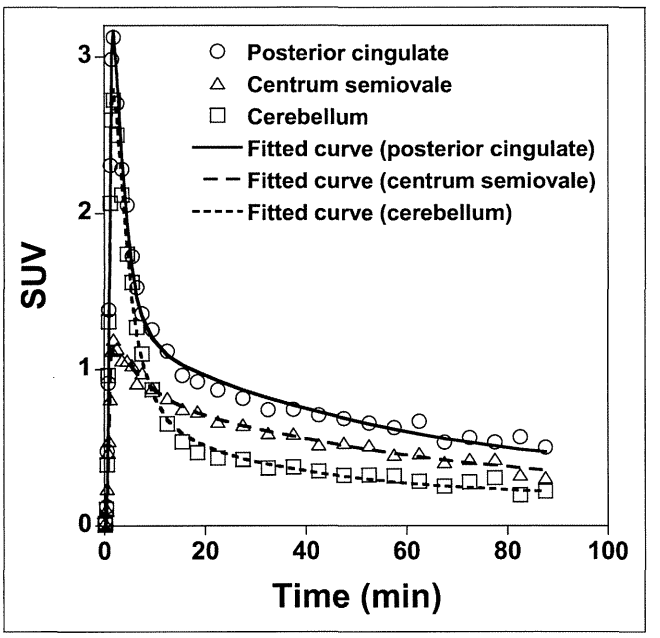

FIGURE 6. Typical time–activity curves in brain regions of AD patient and fitted curves obtained using standard 2-tissue-compartment model.

TABLE 2
Kinetic Parameters Obtained by 2-Tissue-Compartment Model Analysis of ^{11}C-AZD2184 Binding in Control Subjects

Brain region	K_1 (mL/mL/min)	k_2 (min^{-1})	k_3 (min^{-1})	k_4 (min^{-1})	V_T (mL/mL)	*DVR*
Frontal cortex	0.23 ± 0.07	0.42 ± 0.09	0.05 ± 0.02	0.05 ± 0.02	1.14 ± 0.19	0.99 ± 0.07
Temporal cortex	0.25 ± 0.07	0.42 ± 0.09	0.06 ± 0.02	0.05 ± 0.02	1.22 ± 0.17	1.07 ± 0.06
Parietal cortex	0.25 ± 0.06	0.43 ± 0.08	0.05 ± 0.02	0.05 ± 0.02	1.18 ± 0.17	1.03 ± 0.09
Occipital cortex	0.32 ± 0.07	0.53 ± 0.12	0.05 ± 0.02	0.04 ± 0.01	1.28 ± 0.17	1.12 ± 0.09
Hippocampus	0.22 ± 0.05	0.41 ± 0.12	0.08 ± 0.04	0.06 ± 0.02	1.27 ± 0.19	1.11 ± 0.07
Posterior cingulate	0.32 ± 0.09	0.52 ± 0.11	0.06 ± 0.03	0.06 ± 0.03	1.33 ± 0.23	1.16 ± 0.11
Centrum semiovale	0.09 ± 0.03	0.17 ± 0.08	0.09 ± 0.04	0.05 ± 0.01	1.50 ± 0.31	1.30 ± 0.12
Cerebellum	0.28 ± 0.06	0.38 ± 0.05	0.03 ± 0.02	0.05 ± 0.02	1.15 ± 0.22	—

Values are mean ± SD.

The rate constants and related kinetic parameters for ^{11}C-AZD2184 binding in control subjects and AD patients are given in Tables 2 and 3, respectively. In control subjects, the V_T in cerebral cortical regions was similar to that in the cerebellum. In AD patients, V_T values were consistently higher in cerebral cortical regions than in the cerebellum. The V_T and the *DVR* in cerebral cortical regions were significantly higher in AD patients than in control subjects (unpaired *t* test, $P < 0.01$). The *DVR* in the centrum semiovale was more than 1 in average for both control subjects and AD patients. No significant differences in V_T and *DVR* were observed for the centrum semiovale between control subjects and AD patients.

The *SUVR* and *DVR* in control subjects and AD patients are shown in Table 4. The *SUVR* for each integration interval was at the same level and in agreement with the corresponding *DVR* value. *SUVR* and *DVR* in cerebral cortical regions were significantly higher in AD patients than in control subjects. The relationship between *DVR* and *SUVR* is shown in Figure 7. Significant correlations were observed between *DVR* and *SUVR* for each integration interval.

DISCUSSION

In the present examination of ^{11}C-AZD2184 binding to amyloid-β deposits, there was high binding in the cerebral cortical regions of AD patients in comparison with control subjects, the same as in a previous report (*7*). The *DVR* values of ^{11}C-AZD2184 in cerebral cortical regions for both control subjects and AD patients were almost the same level as those of ^{11}C-PIB reported previously (*18*). Although previously developed radioligands, such as ^{11}C-PIB, show high nonspecific binding in white matter, the white matter binding was not conspicuous for ^{11}C-AZD2184. The *SUV*s in the white matter were less than 0.5 after 60 min of injection of ^{11}C-AZD2184 in both control subjects and AD patients, and those of ^{11}C-PIB were reported to be more than 1 (*4*). The regional time–activity curves could be described by the standard 2-tissue-compartment model. The dissociation rate constant k_4 was 0.04–0.05 min^{-1}, not zero, indicating reversibility of binding. Thus, it was evident that the kinetic behavior of ^{11}C-AZD2184 is similar to that of established neuroreceptor ligands such as ^{11}C-raclopride (*20*) and that this radioligand is likely suitable for quantitative analyses using various established approaches.

The white matter binding of ^{11}C-AZD2184 appears lower than that reported for other amyloid radioligands such as ^{11}C-PIB (*4*), the same as in the previous autoradiographic study with postmortem brain (*6*). In control subjects, there was no obvious difference between binding in gray and white matter. However, kinetic analysis revealed the *DVR* to be more than 1 (~1.3–1.5) in the centrum semiovale, a region that almost entirely consists of white matter, for both control subjects and AD patients. The nature of the binding of amyloid ligand to white matter is not fully understood. It has been reported that ^{11}C-PIB may bind to myelin, which is organized in a β-sheet structure in the same way as amyloid-β deposits (*21–23*). The proposed binding has low affinity and is likely not saturable because of the large amount of myelin in the brain. In other words, a high concentration of unlabeled ligand would be required to saturate the binding of amyloid

TABLE 3
Kinetic Parameters Obtained by 2-Tissue-Compartment Model Analysis of ^{11}C-AZD2184 Binding in AD Patients

Brain region	K_1 (mL/mL/min)	k_2 (min^{-1})	k_3 (min^{-1})	k_4 (min^{-1})	V_T (mL/mL)	*DVR*
Frontal cortex	0.21 ± 0.04	0.27 ± 0.08	0.09 ± 0.02	0.04 ± 0.01	2.49 ± 0.48	1.96 ± 0.25
Temporal cortex	0.22 ± 0.05	0.27 ± 0.09	0.08 ± 0.01	0.04 ± 0.01	2.48 ± 0.43	1.97 ± 0.26
Parietal cortex	0.18 ± 0.05	0.25 ± 0.10	0.07 ± 0.02	0.04 ± 0.01	2.30 ± 0.47	1.84 ± 0.37
Occipital cortex	0.28 ± 0.05	0.39 ± 0.10	0.07 ± 0.02	0.03 ± 0.01	2.35 ± 0.54	1.86 ± 0.33
Hippocampus	0.21 ± 0.03	0.32 ± 0.08	0.07 ± 0.02	0.04 ± 0.02	1.81 ± 0.33	1.43 ± 0.15
Posterior cingulate	0.26 ± 0.06	0.30 ± 0.10	0.08 ± 0.02	0.04 ± 0.01	3.04 ± 0.77	2.39 ± 0.42
Centrum semiovale	0.10 ± 0.02	0.14 ± 0.03	0.08 ± 0.05	0.05 ± 0.03	1.94 ± 0.54	1.51 ± 0.22
Cerebellum	0.28 ± 0.05	0.37 ± 0.08	0.03 ± 0.02	0.06 ± 0.05	1.27 ± 0.20	—

Values are mean ± SD.

TABLE 4
*SUVR*s of ^{11}C-AZD2184 in Control Subjects and AD Patients

	Control				AD			
	SUVR				*SUVR*			
Brain region	20–40 min*	40–60 min*	60–90 min*	*DVR*	20–40 min*	40–60 min*	60–90 min*	*DVR*
Frontal cortex	1.04 ± 0.04	1.07 ± 0.09	0.99 ± 0.10	0.99 ± 0.07	2.16 ± 0.28†	2.17 ± 0.27†	2.13 ± 0.28†	1.96 ± 0.25†
Temporal cortex	1.10 ± 0.04	1.14 ± 0.04	1.08 ± 0.07	1.07 ± 0.06	2.09 ± 0.23†	2.14 ± 0.25†	2.15 ± 0.30†	1.97 ± 0.26†
Parietal cortex	1.06 ± 0.07	1.08 ± 0.10	1.03 ± 0.09	1.03 ± 0.09	1.93 ± 0.30†	1.98 ± 0.38†	2.01 ± 0.44†	1.84 ± 0.37†
Occipital cortex	1.13 ± 0.06	1.21 ± 0.08	1.11 ± 0.10	1.12 ± 0.09	1.87 ± 0.38†	1.97 ± 0.33†	2.01 ± 0.38†	1.86 ± 0.33†
Hippocampus	1.15 ± 0.07	1.18 ± 0.05	1.15 ± 0.07	1.11 ± 0.07	1.52 ± 0.11†	1.52 ± 0.15†	1.58 ± 0.16†	1.43 ± 0.15†
Posterior cingulate	1.19 ± 0.08	1.24 ± 0.13	1.17 ± 0.12	1.16 ± 0.11	2.46 ± 0.44†	2.54 ± 0.43†	2.56 ± 0.42†	2.39 ± 0.42†
Centrum semiovale	1.41 ± 0.08	1.49 ± 0.14	1.36 ± 0.17	1.30 ± 0.12	1.68 ± 0.19	1.72 ± 0.21	1.64 ± 0.22	1.51 ± 0.22

*Integration interval.
†Significant differences from normal control subjects (unpaired *t* test, $P < 0.01$).
Values are mean ± SD.

radioligands to cerebral white matter (*24*). Moreover, it has been estimated that ROIs defined for the cerebral cortex contain about 60% of gray matter and 30% of white matter (*25*). This tissue heterogeneity may affect ^{11}C-AZD2184 binding in the cerebral cortices.

To examine simplified approaches for quantification of ^{11}C-AZD2184 binding, the *SUVR* was calculated using the cerebellum as a reference brain region, with integration intervals of 20–40, 40–60, and 60–90 min. The *SUVR* of each integration interval was at the same level and statistically in good agreement with the *DVR* values obtained by kinetic analysis, although systemic overestimations in *SUVR* were observed. This cross-validation indicates that ^{11}C-AZD2184 binding can be estimated using a short scanning time and no arterial blood sampling. The nonlinearity and bias of *SUVR* as compared with *DVR* are observed in most radiotracers (*26,27*). However, the fast relative equilibrium of ^{11}C-AZD2184 could be one of the main advantages over ^{11}C-PIB (*4*). In further study, systemic errors in *SUVR* of ^{11}C-AZD2184 should be investigated with simulation studies. Although all integration intervals can be used to calculate *SUVR*, integration intervals of 40–60 and 60–90 min might be more preferable because the early part of the time–activity curve is generally affected by changes in K_1 due to changes in cerebral blood flow (*20*). However, a lack of an early phase of PET data might hamper an adequate coregistration between PET and MR images, especially in control subjects because of a low binding in the white matter.

It has been reported that synaptic loss is associated with nondiffuse plaques, but not with diffuse plaques (*28*), and that the neuropathology in AD is characterized by cortical neuritic plaque containing dense-cored amyloid deposition (*29*). ^{11}C-BF227, a recently developed radiotracer for in vivo imaging of amyloid-β, has been considered to bind more preferentially to dense-cored amyloid deposition than ^{11}C-PIB (*19*). Further research is needed to demonstrate the binding characteristics of ^{11}C-AZD2184 in different types of amyloid plaque.

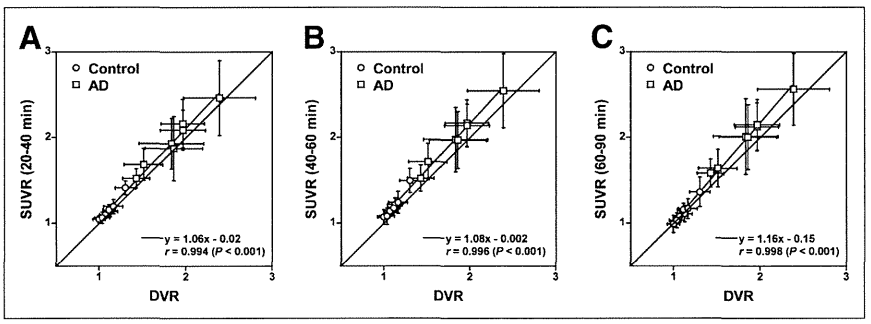

FIGURE 7. Relationship between *DVR* and *SUVR* for integration intervals of 20–40 min (A), 40–60 min (B), and 60–90 min (C). Respective data indicate mean and SD of each ROI.

CONCLUSION

The novel radioligand ^{11}C-AZD2184 provides high-contrast imaging of amyloid-β deposits in brain. The regional kinetics of ^{11}C-AZD2184 binding in control subjects and AD patients could be described by the standard 2-tissue-compartment model. The *SUVR* calculated from integrated time–activity curves in targeted and reference brain regions can be used as an index of ^{11}C-AZD2184 binding for clinical investigations without arterial input function.

DISCLOSURE

The costs of publication of this article were defrayed in part by the payment of page charges. Therefore, and solely to indicate this fact, this article is hereby marked "advertisement" in accordance with 18 USC section 1734. This study was supported in part by the "Japan Advanced Molecular Imaging Program (J-AMP)" of the Ministry of Education, Culture, Sports, Science and Technology (MEXT), Japanese Government, and a grant-in-aid for Comprehensive Research on Dementia (no. 11103404) from the Ministry of Health, Labor and Welfare. No other potential conflict of interest relevant to this article was reported.

ACKNOWLEDGMENTS

We thank Katsuyuki Tanimoto, Takahiro Shiraishi, Kazuko Suzuki, and Izumi Izumida for their assistance in the PET experiments. 5-(6-{[tert-butyl(dimethyl)silyl]oxy}-1,3-benzothiazol-2-yl)pyridin-2-amine (AZD2184) and its precursor 5-(6-(tert-butyldimethylsilyloxy)benzo[d]thiazol-2-yl)pyridin-2-amine were kindly provided by AstraZeneca R&D, Södertälje, Sweden.